

Detailed study of an efficient blue laser source by second-harmonic generation in a semimonolithic cavity for the cooling of strontium atoms

Bruce G. Klappauf, Yannick Bidel, David Wilkowski, Thierry Chanelière, and Robin Kaiser

We have constructed a blue laser source consisting of an amplified, grating tuned diode laser that is frequency doubled by a KNbO_3 crystal in a compact standing wave cavity and produces as much as 200 mW of internal second-harmonic power. We have analyzed the unusual characteristics of this standing wave cavity to clarify the advantages and disadvantages of this configuration as an alternative to a ring cavity for second-harmonic generation. We emphasize its efficiency and stability and the fact that it has an inherent walk-off compensation, similar to twin crystal configurations. We demonstrate its utility for laser cooling and trapping of earth alkalis by stabilizing the laser to the 461-nm transition of strontium, using a heat pipe, and then forming a magneto-optic trap of strontium from a Zeeman-slowed atomic beam. © 2004 Optical Society of America

OCIS codes: 020.0020, 140.0140, 190.0190, 230.0230.

1. Introduction

The advancement of laser cooling and trapping has progressed to include an increasing variety of elements that involve a broad spectrum of wavelengths. In particular, there has been a great deal of interest lately in the earth alkalis because of the existence both of narrow intercombination transitions to the triplet states (interesting for metrology and laser cooling) and for the $J = 0$ ground state of some abundant isotopes (interesting for collision and scattering studies).^{1–10} For Ca and Sr, however, the primary cooling transition is in the blue spectral region, and Mg uses both blue and UV transitions. In addition, the relatively large scattering rate of these primary trapping transitions, with the associated high saturation intensities, means that higher powers would be needed to optimize the magneto-optic trap (MOT). Whereas

many alkalis can be trapped with diode lasers or Ti:sapphire lasers, there are few powerful, reliable, and tunable single-mode sources in the shorter wavelengths. It is therefore common to perform second-harmonic generation (SHG) on these more readily available sources, but to obtain enough second-harmonic power one must either have a highly efficient SHG process or have enough fundamental power to compensate for the low SHG efficiency.

Because of the low value of second-order nonlinearity, even in the best crystals high single-pass efficiency demands either extremely high intensities or unfeasible interaction lengths. This problem is overcome by use of a buildup cavity that allows even modest fundamental powers to generate high intensities and relatively efficient SHG, which are most commonly seen in the form of ring cavities such as the familiar bow-tie cavity. Commercial examples of these tunable cavities are available, but generally less efficiency is claimed for them than for the system presented here. Additionally, there are many new solid-state systems with intracavity frequency doubling, but these systems are available only at specific wavelengths. Perhaps it is because of the familiarity of ring cavities that the advantages of a small, single-exit, monolithic or semimonolithic standing wave cavity have been largely overlooked, despite the demonstration of record efficiency (>80%) and cw

B. G. Klappauf (bgk@orc.soton.ac.uk) is with the Optoelectronic Research Centre, University of Southampton, Southampton SO17 1BJ, England. Y. Bidel, D. Wilkowski, T. Chanelière, and R. Kaiser are with the Laboratoire Ondes et Désordre, 1361 Route des Lucioles, 06560 Valbonne, France.

Received 19 August 2003; revised manuscript received 22 December 2003; accepted 2 February 2004.

0003-6935/04/122510-18\$15.00/0

© 2004 Optical Society of America

second-harmonic (SH) power (>500 mW at 473 nm).^{11,12}

We have constructed and analyzed such a cavity at 461 nm for our Sr MOT, using a KNbO_3 crystal, and have found it well suited for laser cooling experiments in the blue spectral region. We describe our design of this cavity and of its performance. Its tuning and output field characteristics are quite different from those of unidirectional single crystal (ring cavities), a bidirectional standing wave,¹³ or even bicrystal systems¹⁴ and could be quite confusing for a nonspecialist who may be constructing such a cavity. To our knowledge, in fact there are only a few journal publications that briefly allude to the full range of behavior that one can expect in this case.^{12,15} Therefore we also present an analysis of the design both to clarify the possible advantages of a single-sided semimonolithic standing wave cavity in terms of stability, efficiency, and cost and to aid the nonspecialist reader in reproducing and understanding such a cavity for similar applications.

The main drawback of this configuration is the possibility of a large relative phase shift introduced between the fundamental and the SH wavelengths by the high-reflection (HR) coating on the crystal¹⁵ and the lobed output when the crystal is tuned away from phase matching. It has been shown, however, that this problem can be avoided by the use of properly designed coatings, and, as we reiterate here, whereas a nonzero phase shift of the cavity mirror may reduce the ideal performance, it can be compensated for to a large degree by minor temperature tuning of the crystal to maintain an advantage even in the worst case.^{12,16,17} Finally, we point out that this cavity inherently includes a walk-off compensation mechanism similar to those of the two crystal systems extensively studied by others but without the complicated alignment and orientation issues.^{14,18–21}

This paper is organized as follows: Section 2 gives a general description of the cavity for reference in the rest of the paper. It includes basic formulas with which we analyze and optimize the cavity. In Section 3 we compare calculations based on integration of the coupled paraxial-wave equations to those of a greatly simplified approximation. The approximations are shown to give reasonable results for practical cases (if the angular bandwidth of the system is not too small) and, because of their simplicity, provide a simple means of predicting and understanding the tuning and power characteristics of the cavity. In Section 4 we describe the experimental setup and show the results of measurements of the cavity output characteristics. We put our actual values into the general discussions of Sections 2 and 3 and compare these with our measurements. We conclude in Section 5 with a summary and suggestions for extending this research, and we include an appendix designed to provide all the information necessary for calculating parameters for similar cavities.

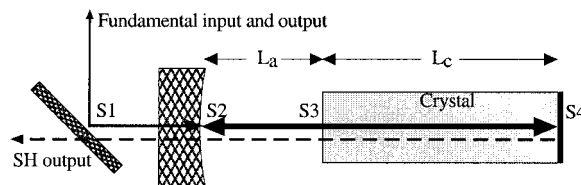


Fig. 1. Schematic of singly resonant cavity design, showing the path of the fundamental and the SH waves. Surfaces are S1, dichroic beam splitter; S2, spherical mirror input coupler; S3, AR surface coated for both wavelengths; S4, HR surface coated for both wavelengths.

2. Description of the Cavity

The semimonolithic standing wave cavity, resonant for the fundamental wavelength, was chosen both because of its demonstrated efficiency and because of its economy in terms of space and costs. It consists of a KNbO_3 crystal and a spherical mirror configured as shown in Fig. 1 to build up the fundamental field intensity and hence the conversion efficiency. The SHG in the resonating cavity can then be treated as a single-pass case but with an enhanced fundamental circulating power, P_c .^{22,23} Specific parameters for our setup are given in Section 4.

A. Behavior

One of the polished ends of the crystal (S4; Fig. 1) is HR, coated and the other end (S3) is antireflection (AR) coated; each coating is for both the fundamental and the SH wavelengths. The spherical mirror input coupler (S2) facing the AR face of the crystal has a reflectivity R_c for the fundamental and is AR coated for the SH. The flat face is doubly AR coated. A similarly treated beam splitter (S1) before the mirror directs the fundamental into the cavity and again allows the SH to exit. Unlike in ring cavities, the fundamental passes through the crystal twice per cavity round trip, allowing for the possibility of nearly four times the round-trip conversion efficiency, even in walk-off limited cases, as we detail in Section 3.

The power transmission and reflection equations for this cavity with respect to round-trip parasitic loss \mathcal{L} , round-trip SH conversion factor $C = P_{2\omega}/P_c = \gamma P_c$, and input coupler reflectivity R_c are equivalent to that of a ring cavity with an effective optical path of $2L_p$, where $L_p = L_a + nL_c$ (see Fig. 1). P_c is the circulating fundamental power entering the crystal at S3 (i.e., one of the counterpropagating waves that compose the standing wave), n is the index of refraction, and γ , normally expressed in inverse kilowatts, is a power-independent figure of merit for a given geometric SHG configuration (i.e., including the crystal parameters and fundamental beam parameters). One readily arrives at equations for the relative reflectivity $R \equiv P_r/P_{in}$ and transmission $T \equiv P_t/P_{in}$, where P_{in} , P_r , and P_t are, respectively, the incoming fundamental power, the reflected fundamental power, and the transmitted fundamental power. $T_m = 1 - R_m \approx 0$ is the transmission of mirror face

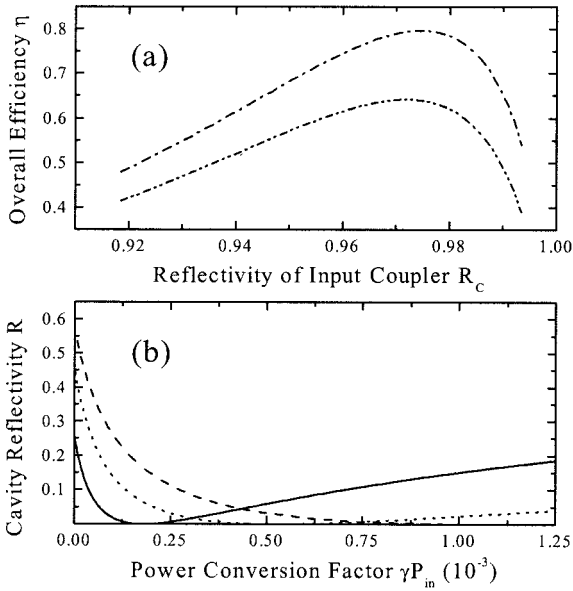


Fig. 2. Typical on-resonance reflection coefficients, R versus γP_{in} for $\mathcal{L} = 0.5\%$ and input couplers $R_c = 96.5\%$ (dashed curves), 97.5% (dotted curve), and 98.5% (solid curve). (a) Dependence of overall conversion efficiency $\eta = P_{2\omega}/P_{in}$ on input coupler reflectivity for $\gamma P_{in} = 0.522 \times 10^{-3}$ and $\mathcal{L} = 0.5\%$ (dashed-dotted curve) and $\mathcal{L} = 1.0\%$ (dashed-double-dotted curve).

S4, and we assume that $\mathcal{L} \ll 1$ and $C \ll 1$, resulting in

$$R = \left| \frac{(1 - \mathcal{L} - C)^{1/2} \exp(i2k_0 L_p) - R_c^{1/2}}{1 - [R_c R_m (1 - \mathcal{L} - C)]^{1/2} \exp(i2k_0 L_p)} \right|^2, \quad (1)$$

$$T = \left| \frac{[(1 - R_c) T_m (1 - \mathcal{L} - C)^{1/2}]^{1/2}}{1 - [R_c (1 - \mathcal{L} - C)]^{1/2} \exp(i2k_0 L_p)} \right|^2, \quad (2)$$

where $k_0 = 2\pi/\lambda = \omega/c$ is the fundamental vacuum wave vector. The definitions and approximations given above can be solved numerically for any parameter from the equation

$$C\{1 - [R_c R_m (1 - \mathcal{L} - C)]^{1/2}\}^2 = \gamma P_{in} (1 - R_c), \quad (3)$$

where we treat the power-conversion factor γP_{in} as a convenient dimensionless parameter for graphing cavity behavior, allowing one more easily to generalize and compare different experiments.

By measuring scans of the transmission and reflection as a function of the input power we determine the actual values of \mathcal{L} and C as well as the fraction ϵ of P_{in} that is mode matched to the cavity. Figure 2(a) shows the dependence of total efficiency $\eta = P_{2\omega}/P_{in} = C^2/\gamma P_{in}$ on the input coupler's reflectivity and Fig. 2(b) shows cavity reflectivity R versus the power-conversion factor. The y intercepts in Fig. 2(b) give the parasitic loss, and the power dependence gives γ , either by curve fitting or by passing the minimum where $R_c^{opt} \sim 1 - (\mathcal{L} + C)$. For an experimental curve, a nonzero value of the minimum would indicate that $\epsilon < 1$, as one can see from our data in Subsection 4.D below. Additional nonlinear losses

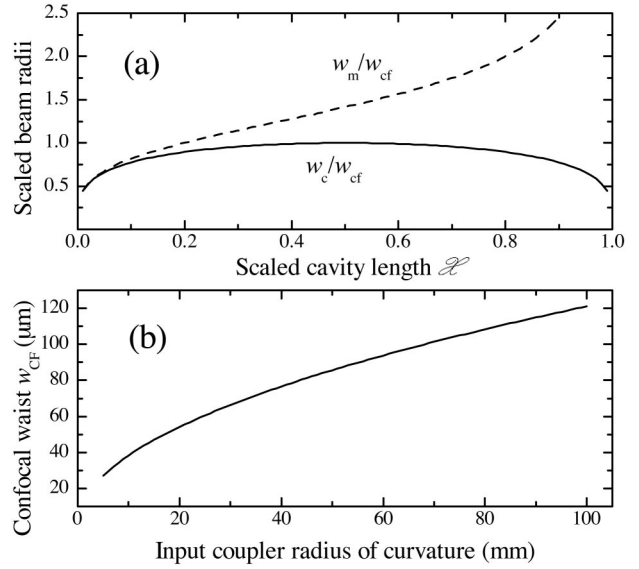


Fig. 3. (a) Beam radii at the crystal face and at the input coupler scaled to confocal value w_{cf} at the crystal face as a function of scaled cavity length \mathcal{L} . (b) Corresponding confocal waist versus \mathcal{R} .

may need to be added to \mathcal{L} as well (see Subsection 4.B). Figure 2 indicates that deviations from R_c^{opt} of $\leq 0.5\%$ are not critical.

B. Mode

The radii of the beam (radius where the intensity drops to e^{-2} of the central intensity) at crystal face S4 and at input mirror S2 are given, respectively, by

$$w_c = \left\{ \frac{\lambda \mathcal{R}}{\pi} [\mathcal{L}(1 - \mathcal{L})]^{1/2} \right\}^{1/2}, \quad (4)$$

$$w_m = \left[\frac{\lambda \mathcal{R}}{\pi} \left(\frac{\mathcal{L}}{1 - \mathcal{L}} \right)^{1/2} \right]^{1/2}, \quad (5)$$

where $\mathcal{L} = (L_a + L_c/n)/\mathcal{R}$ is the scaled cavity length and \mathcal{R} is the input coupling mirror's radius of curvature (ROC). The confocal waist at crystal face S4 is given by $w_{cf} = w_c(\mathcal{L} = 0.5) = [\lambda \mathcal{R}/2\pi]^{1/2}$. Figure 3(a) shows the scaled beam radii w_c/w_{cf} and w_m/w_{cf} versus \mathcal{L} . We see that over most of the stable range of the cavity the beam radius at S4 remains near w_{cf} , whose dependence on \mathcal{R} is shown in Fig. 3(b). Additionally, operation on the two extremes where w_{cf} would decrease significantly is impeded by increasing instability as $\mathcal{L} \rightarrow 1$ and by the crystal length itself as $\mathcal{L} \rightarrow 0$.

This makes cavity design extremely simple because no $ABCD$ matrix analysis need be done, nor does one have to worry about coma as for ring cavities.²⁴ The desired waist determines the mirror's ROC; then one can simply change the cavity length to adjust almost independently the beam diameter on the input coupler, the cavity's free spectral range (FSR), the level of transverse mode degeneracy (degenerate at $\mathcal{L} = 0.5$ and $\mathcal{L} = 1$), or the crystal beam waist to some degree. Note that for this cavity the

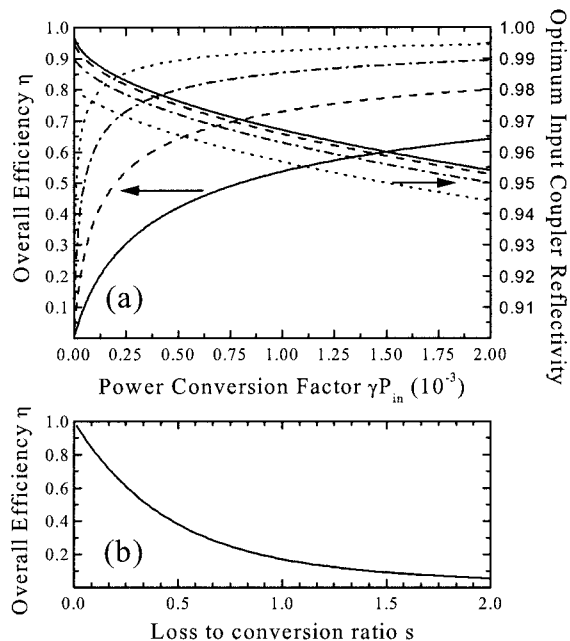


Fig. 4. (a) Comparison of overall efficiency (rising curves, left scale) and optimum input coupler reflectivity (descending curves, right scale) versus power-conversion factor for various parasitic loss values: $\mathcal{L} = 0.25\%$ (dotted curves), 0.5% (dashed-dotted curves), 1.0% (dashed curves), and 2% (solid curves). (b) Ratio s of efficiency versus loss to conversion [from Eq. (6)].

transverse mode spacing at $\mathcal{L} = 0.5$ is $FSR/4 = c/8L_p$, so all modes designated TEM_{mn} with indices $m + n = 4q$, where m , n , and q are the transverse y , transverse z , and longitudinal mode indices of the resonant field, respectively, will be superimposed on the TEM_{00} resonance. Therefore a value of \mathcal{L} on either side of 0.5 will separate the modes that are visible in a scan of the cavity without changing the other parameters drastically, thus permitting easier mode matching of the input beam.

C. Optimization

Whereas the equations above are useful for analyzing cavity operation, for optimization purposes we assume optimum coupling conditions and perfect mode matching ($R = 0$ and $\epsilon = 1$) such that all the power is absorbed by loss or conversion ($\mathcal{L} + C$) in the cavity. The finesse is then given approximately by the Fabry-Perot equation $F = \pi(R_c^{opt})^{1/2}/(1 - R_c^{opt})$ from the full width at half-maximum (FWHM) of the transmission equation. In this case the total efficiency is

$$\eta = [(s^2 + 1)^{1/2} - s]^2, \quad (6)$$

where $s \equiv \mathcal{L}/[2(\gamma P_{in})^{1/2}] = \mathcal{L}\eta^{1/2}/(2C)$, which can be approximated for $\mathcal{L} + C \ll 1$ by

$$\eta \approx \frac{C}{\mathcal{L} + C} \stackrel{\mathcal{L} \ll C}{\approx} \frac{1}{1 + s}. \quad (7)$$

From relation (7) it is clear that loss and the power-conversion factor are the key parameters for resonant

cavity SHG. Equation (6) is shown versus s in Fig. 4(b), where we see that high efficiency ($>80\%$) requires the loss of less than one fifth of the conversion, which generally means $\mathcal{L} < 1\%$. It is a bit easier to see the effect of experimental parameters (\mathcal{L} , γP_{in}) if we plot the efficiency versus γP_{in} for various losses as shown in Fig. 4(a). The associated optimum coupling value for each case is shown as well. Figure 4 shows that increasing γP_{in} at the cost of higher loss (for example, by lengthening the crystal or decreasing the waist at the cost of increased linear or nonlinear absorption) may actually decrease overall efficiency.

To account for this maximum in the overall efficiency an initial optimization procedure might be first to determine the expected input power available, to choose a target value for γ of, for example, $10^{-3}/P_{in}$, and then, based on information in Subsections 4.B and 4.C below, choose a length and a waist to minimize the loss while we use the calculations of Section 3 to ensure that γ remains above the chosen value. Once the desired beam waist and crystal length have been chosen, the coupler is determined and the length can be fixed or adjusted as necessary based on information in this section and Subsection 4.C below.

Figure 4 highlights the advantages of the semimonolithic cavity. First, with only two exposed intracavity optical surfaces, the potential for passive loss is much less. Second, the potential for enhanced nonlinear conversion described in Section 3 may increase the efficiency directly for $\gamma P_{in} \ll 10^{-3}$ or indirectly by relaxing the length or the waist constraints, which could reduce the overall loss (increasing η) for $\gamma/P_{in} > 10^{-3}$. Note that if linear absorption ($\mathcal{L} \propto L_c$) were the only loss, the semimonolithic cavity would not improve the efficiency compared with that for a single-pass cavity. Because the double-pass cavity will at best quadruple γ while it doubles the length, we can see that $s = \mathcal{L}/[2(\gamma P_{in})^{1/2}] = 2\mathcal{L}/[2(4\gamma P_{in})^{1/2}]$, and hence the efficiency, will remain the same. Such is seldom the case, but the point is clear that the often highlighted $4\times$ increase in γ does not mean a $4\times$ increase in SH power.

The optimization of γ for a Gaussian beam has been thoroughly treated by Boyd and Kleinman,²² with implications for cavities given by Ashkin *et al.*²³ We need include only the effects of the interference between the forward- and backward-generated SH fields, as they are now superimposed.

This interference has been the subject of several studies.^{11,15,16,25} It has been noted that the phase shift between the forward and backward fields can reduce or enhance γ by a factor of 0 to 4 times that of the single-pass value. To our knowledge no one has pointed out the connection between this configuration and the much-studied effect of walk-off compensation with reverse oriented crystal pairs.^{14,19-21} If we unfold the cavity in Fig. 1 we see that it appears as in Fig. 5 as two crystals that are (apart from the dielectric coating between them) in optical contact, with the

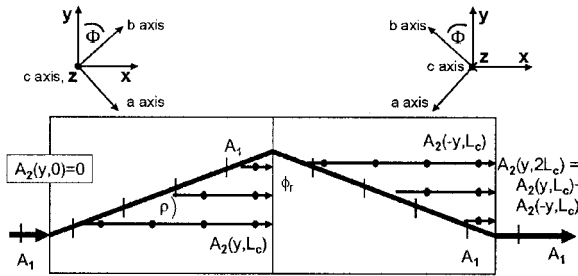


Fig. 5. Effective propagation path for the circulating fundamental and the SH in the unfolded cavity with relative phase shift ϕ_r , fundamental walk-off angle ρ , and crystal cut angle Φ . A_1 is the approximately constant, vertically polarized fundamental (slanted, barred lines). $A_2(y, x)$ are horizontally polarized SH (solid lines with filled circles) fields at various points in the propagation as referred to in the text. The output SH field at $x = 2L_c$ is the coherent sum of the contribution produced in each half. Axes show relative orientations of crystal's principal axes for each half.

sign of the walk-off reversed as in the walk-off compensation configuration of Fève *et al.*²¹ However, in this case one needs only to buy, cut, and coat one crystal; then alignment is automatic. Thus, in addition to the other advantages discussed, this configuration is particularly useful when large walk-off is a problem.

We show that, whereas one would ideally like to eliminate the phase shift at the reflective crystal face (through either proper coating or an adjustable compensator), one can always compensate for this phase shift with the overall temperature-dependent phase mismatch Δk to achieve better than double the conversion of the single-pass case.

We consider KNbO₃ in detail because, although it is somewhat delicate, its temperature sensitivity makes it easily tunable and it has been widely used for high-power doubling throughout the blue and green spectra.¹¹ Details of this crystal and of how to calculate the parameters associated with SHG are given in Appendix A.

3. Theory

A. Coupled-Wave Equation

The derivation of the paraxial-wave equation and its application to SHG of Gaussian beams can be found in many nonlinear optics texts.^{26,27} We follow the sign convention of Boyd in that our linearly polarized fundamental and SH fields and the wave-vector mismatch are defined by

$$E_m = \frac{A_m}{2} \exp[i(k_m x - m\omega t)] + \text{c.c.} \quad (m = 1, 2), \quad (8)$$

$$\Delta k = 2k_1 - k_2, \quad (9)$$

respectively, such that the intensity is given in MKS units by

$$I_m = \frac{\epsilon_0 n_m c}{2} |A_m|^2. \quad (10)$$

Choices of coordinate axes are shown in Fig. 5 for each half of the unfolded cavity. $A_m(\mathbf{r})$ is assumed to be slowly varying relative to length scales of λ , $k_m = m\omega n_m/c$ is the x -aligned wave vector, and $\mathbf{r} = \{x, y, z\}$ is the standard position vector. Applying Maxwell's equations to a nonlinear, anisotropic medium (with the approximation of zero absorption), we find the nonlinear coupled-wave equations for the fundamental and SH fields, respectively, at a position \mathbf{r} in the nonlinear medium given by

$$\frac{\partial A_1(\mathbf{r})}{\partial x} = \frac{i}{2k_1} \left[\nabla_t^2 A_1(\mathbf{r}) + i2k_1 \rho \frac{\partial A_1(\mathbf{r})}{\partial y} \right] + \frac{ik_1}{n_1^2} dA_1^*(\mathbf{r})A_2(\mathbf{r})\exp(-i\Delta kx), \quad (11)$$

$$\frac{\partial A_2(\mathbf{r})}{\partial x} = \frac{i}{2k_2} \nabla_t^2 A_2(\mathbf{r}) + \frac{ik_2}{2n_2^2} dA_1(\mathbf{r})^2 \exp(i\Delta kx), \quad (12)$$

where the transverse Laplacian is given by $\Delta_t^2 = \partial^2/\partial y^2 + \partial^2/\partial z^2$ and * indicates a complex conjugate. These equations are valid for the type I phase-matching interactions (in this case two extraordinary beams giving one ordinary beam, $e + e = o$) described in this paper. Type II equations are dealt with elsewhere.^{14,21}

The equations contain four constants that need to be calculated or measured: the indices for the fundamental and the harmonic, n_1 and n_2 ; walk-off angle ρ ; and second-order nonlinearity $d \equiv d_{\text{eff}}$. These constants will all depend on the crystal orientation, which will be determined by phase-matching angle Φ for the chosen temperature and wavelength. Appendix A shows the calculations of these constants as functions of temperature and wavelength so the reader can determine them for various situations.

These equations are integrated through twice the crystal length, as depicted in Fig. 5, with variable phase shift ϕ_r , and reversal of the walk-off inserted at the half-way point. ϕ_r accounts for the relative phase shift between A_1 and A_2 that is due to the dielectric mirror. Note that, as opposed to cavities with the mirrors independent of the crystal, angle tuning in this cavity is not possible, and the position of the waist is fixed at the mirrored surface (the center point in Fig. 5). Another difference from other cases is that d_{eff} (Ref. 20) and Δk do not change sign on reflection: Only the sign of the walk-off changes. The relation of the lab coordinates to the crystallographic axes for the forward and reflected halves is indicated by the two insets of Fig. 5. See Appendix A for further details. The integration routine follows the example of Fève *et al.*²¹ Recall that A_1 will

be the field associated with fundamental power P_c entering the crystal at surface S3.

B. Semianalytic Equation

In most practical cases, with Gaussian beams and low single-pass pump depletion ($<5\%$), actual integration of the coupled-wave equations is not necessary for reasonable reproduction of experimental results. One often replaces these equations with heuristic equations that involve a single integral.^{21,22} We find that, in our case, because we intentionally work in the weak-focusing regime [$L_c < z_0 = \lambda/(\pi w_0^2)$] for reasons discussed in Subsections 4.B and 4.C below, further approximations allow for an even simpler single-integral solution. In addition to reasonably reproducing both the power and the beam profile by use of any standard math software, it also provides some analytical insight to help in understanding the important characteristics of this SHG process.

The nondepleted pump approximation with the assumption of a Gaussian pump beam allows us to eliminate Eq. (11) and use for $A_1(\mathbf{r})$ the well-known analytical function for Gaussian propagation. One must account for the walk-off by replacing y in $A_1(\mathbf{r})$ with $y \rightarrow y - \rho x$. This results essentially in what is known as a heuristic equation. To simplify it even further, we make the approximation that weak focusing allows us to ignore diffraction and assume the same Gaussian profile (apart from the translation in y) for propagation through the crystal. Thus

$$A_1(\mathbf{r}) = E_0 \exp\left\{-\frac{z^2}{w_0^2} - \frac{[y - \rho x + (\rho L/2)]^2}{w_0^2}\right\} \quad (13)$$

can be put directly into Eq. (12) (from which the ∇^2 diffraction term has been removed) and the result integrated over x , y , and z . Before continuing it is important to point out here that this formulation was chosen such that the translation effects that are due to walk-off are centered about $y = 0$, so a positive walk-off will produce the same beam profile as a negative walk-off but with the sign of y inverted. So, referring to Fig. 5, field A_2^- from the second half is the same as A_2^+ inverted from the first half and so need not be calculated separately. Putting these conditions together means that the final SH field after the forward and backward passes is just the sum of single-pass field $A_2^+ \equiv A_2(y, z, L_c)$ and its y inversion $A_2^- \equiv A_2(-y, z, L_c)$ with two added phase shifts. Because the phase of the generated SH field is tied directly to the phase of the generating fundamental field, both phase shifts are given in terms of the relative phase shift between the fundamental and A_2^+ that was generated in the first pass. The first phase shift, ϕ_r , was discussed above. The second, $i\Delta k L_c$, accounts for the phase difference accumulated as A_2^+ traverses the crystal a second time relative to the

phase picked up by the fundamental on the first pass. The result is

$$A_2(y, z, 2L_c) = A_2(y, z, L_c) + \exp[i(\Delta k L_c + \phi_r)]A_2(-y, z, L_c). \quad (14)$$

From this, one might expect the resultant power output to have a phase-mismatch tuning curve with a $1 + \cos(\Delta k L_c + \phi_r)$ dependence similar to that described by Fève *et al.*,²¹ and indeed the intensity variation at $y = 0$ does follow, because $A_2^+ = A_2^-$ there. We shall see, however, that this configuration results in an intensity modulation in y that, when it is integrated, gives a more-complex dependence of the total power on the phase mismatch.

Before continuing, we do some scaling and substitutions. We scale the transverse coordinates by fundamental beam waist w_0 and the propagation coordinate by crystal length L_c :

$$\frac{y}{w_0} \rightarrow y, \quad \frac{z}{w_0} \rightarrow z, \quad \frac{x}{L_c} \rightarrow x. \quad (15)$$

Then we define a characteristic parameter β , which is the ratio of the walk-off translation across the crystal ρL_c to SH beam diameter ($2^{1/2}w_0$), integration parameters r and p , and horizontal transverse amplitude function $\mathcal{H}(z)$:

$$\beta = \frac{\rho L_c}{2^{1/2}w_0}, \quad (16)$$

$$r = 8^{1/2}\beta \left(x - \frac{y}{2^{1/2}\beta} - \frac{1}{2}\right), \quad (17)$$

$$p = \frac{\Delta k L_c}{8^{1/2}\beta}, \quad (18)$$

$$\mathcal{H}(z) = \frac{\kappa L_c}{8^{1/2}\beta} \exp(-2z^2), \quad \kappa = \frac{iE_0^2 k_1 d}{n_1^2}. \quad (19)$$

With these substitutions we have for a single pass through the crystal

$$A_2(y, z, L_c) = \mathcal{H}(z) \exp\left(i \frac{\Delta k L_c}{2} + i2yp\right) \times \int_{r_-}^{r_+} dr \exp\left(\frac{-r^2}{2}\right) \exp(ipr), \quad (20)$$

where

$$r_{\pm} = \pm 2^{1/2}\beta - 2y. \quad (21)$$

We can see that the result comprises three parts: Gaussian horizontal transverse amplitude function $\mathcal{H}(z)$, phase function $\Psi(y, \Delta k) = \exp[i\Delta k L_c/2 + i2yp]$ in the exponent, and vertical modulation function $F(y, \Delta k) = \int_{r_-}^{r_+} dr \exp(-r^2/2) \exp(ipr)$ in the form of an easy integral. A simple analysis of this function will help us to understand the results that we shall see below.

To understand the importance of β in this result we

can modify the integral to look like the Fourier transform of a square function Θ of width $8^{1/2}\beta$, offset by $2y$, multiplied by a Gaussian:

$$F(y, \Delta k) = \int_{-\infty}^{\infty} dr \Theta(r, \beta, y) \exp\left(\frac{-r^2}{2}\right) \exp(ipr), \quad (22)$$

where

$$\Theta(r, \beta, y) = \begin{cases} 1 & |r + 2y| \leq 2^{1/2}\beta \\ 0 & \text{otherwise} \end{cases}. \quad (23)$$

Equation (22) presents three characteristic cases for us to examine: $\beta \ll 1$, $\beta \gg 1$, and $\beta \approx 1$.

1. Case I: $\beta \ll 1$

In the limit $\beta \ll 1$, where we have a large beam waist and the translation that is due to walk-off is small, we approximate the plane-wave results found in textbooks. The width of the square function is much smaller than Gaussian width $2^{1/2}$, so we can treat the Gaussian as a constant, $\exp[-(2y/2^{1/2})^2]$. Thus, removing it from the integral, we have the Fourier transform of the offset square function, which is a phase-shifted sinc function [$\text{sinc}(x) \equiv \sin(x)/x$]:

$$\begin{aligned} F(y, \Delta k) &= \exp(-2y^2) \exp(-i2yp) \frac{2 \sin(2^{1/2}\beta p)}{p} \\ &= 8^{1/2}\beta \exp(-2y^2) \exp(-i2yp) \text{sinc}\left(\frac{\Delta k L_c}{2}\right), \end{aligned} \quad (24)$$

giving for the SH field

$$\begin{aligned} A_2(y, z, L_c) &= \kappa L_c \exp[-2(y^2 + z^2)] \\ &\times \exp\left(i \frac{\Delta k L_c}{2}\right) \text{sinc}\left(\frac{\Delta k L_c}{2}\right). \end{aligned} \quad (25)$$

Notice that the y -dependent phase was canceled, leaving, as expected, a Gaussian field of waist $w_0/2^{1/2}$, a flat phase front, and a sinc function phase-matching dependence. The associated intensity has a FWHM of $2\Delta k_{1/2} L_c / \pi = 1.77$.

2. Case II: $\beta \gg 1$

When $\beta \gg 1$ there will be a large walk-off or crystal length, tight focusing, or both. This is a practical case because optimal focusing may easily approach this limit. But we must use caution, as the accuracy of the approximation breaks down somewhat for tight focusing, where $L_c > z_0 = \pi w_0^2 / \lambda$, the Rayleigh length, but this breakdown can be compensated for to a large degree, as we discuss in Subsection 3.D below. For our approximation case II gives a square function much larger than the Gaussian, so for most values of y we simply have the integral of the Gaussian with only a small contribution from the square function near $y = \pm\beta/2^{1/2}$, outside of which the field drops

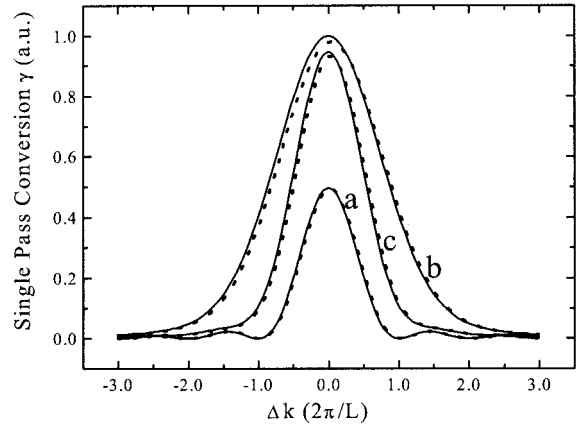


Fig. 6. Comparison of relative SH conversion factor γ calculated by the semianalytic result (solid curves) with that of the heuristic equation (dotted curves) for a single pass through length L_c of the crystal for (a) case I with $\beta = 0.1$, (b) case II with $\beta = 2$, and (c) case III with $\beta = 1$. The vertical scale is arbitrary and serves only to show the change in form because for a given β , L_c and ρ can be chosen to make all three cases visible in the same figure.

rapidly to zero. As the Fourier transform of a Gaussian is a Gaussian, we have (for $|y| < \beta/2^{1/2}$)

$$\begin{aligned} F(y, \Delta k) &= (2\pi)^{1/2} \exp\left(-\frac{p^2}{2}\right) \\ &= (2\pi)^{1/2} \exp\left[-\left(\frac{\Delta k L_c}{4\beta}\right)^2\right], \end{aligned} \quad (26)$$

$$\begin{aligned} A_2(y, z, L_c) &= (2\pi)^{1/2} \mathcal{K}(z) \exp\left(i \frac{\Delta k L_c}{2}\right. \\ &\left. + i2yp\right) \exp\left[-\left(\frac{\Delta k L_c}{4\beta}\right)^2\right], \end{aligned} \quad (27)$$

with a FWHM intensity width $2\Delta k_{1/2} L_c = 8\beta(\ln 2/2)^{1/2} \Rightarrow 2\Delta k_{1/2} L_c / \pi \approx 1.5\beta$, roughly β times larger than in case I. Also, notice that the y -dependent phase remains intact; it is this that will produce the multiple lobes along the y axis for nonzero values of Δk . These lobes are shown in the intensity profiles in Subsection 4.D below.

3. Case III: $\beta \approx 1$

For $\beta \approx 1$ we have the convolution of the Gaussian and the sinc functions, smoothly widening the sinc function and eliminating its distinct minima. Our example is in this regime with $\beta = 1.7$. Considering the two limits, we may suppose a standard convolution function for the width and use $2\Delta k_{1/2} L_c / \pi = [(1.77)^2 + (1.5\beta)^2]^{1/2}$, which seems to work well.

Figure 6 shows the single-pass tuning curve for the three values $\beta = 0.17$, $\beta = 0.43$, and our case $\beta = 1.7$, calculated both with Eq. (20) and with the heuristic equation of Boyd and Kleinman²² (in which they include a waist position parameter μ that we set as 1). We can see the smoothing of the nodes and the enlargement of the tuning bandwidth as β increases. We can also see that in this range our approximation

works quite well. Thus we can quite simply understand what the double-pass power tuning curve will be for each case.

C. Second-Harmonic Power-Tuning Curves

Now we consider the interference effects that the reflection will have on the tuning curve that one would obtain by measuring the total SH output power as a function of the crystal temperature or, equivalently, of phase mismatch Δk . We integrate analytically the output intensity profile I_2 from Eq. (10) over y and z for cases I and II, using the appropriate equations for the fields in each case. We apply case III to our experiment in Section 4.

For case I the single-pass field is symmetric in y and therefore $A_2^+ = A_2^-$, so from Eqs. (10), (14), and (25) we get a power function of the form

$$P^I(\Delta k L_c) = P_0^I \text{sinc}^2\left(\frac{\Delta k L_c}{2}\right) 2[1 + \cos(\Delta k L_c + \phi_r)], \quad (28)$$

where $P_0^I = (\epsilon_0 n_m c / 2) |\kappa L_c \omega_0 \pi^{1/2} / 2|^2$ is the maximum single-pass power at $\Delta k = \phi_r = 0$ and the cosine term has the same oscillation period $\Delta k L_c = 2\pi$ as the sinc^2 term, except at $\Delta k = 0$, where the sinc^2 function has a missing node. Indeed, in this case we see 100% modulation of the power as in Ref. 21 and the same sinc^2 envelope width because they result from the single-pass field but with only half of the frequency in the interference modulation. This is so because by temperature tuning we keep the same Δk in both halves, where in the angle-tuning case the change in the sign of Δk doubles the relative phase shift between the two halves that appears in the cosine.

For case II, by replacing Eq. (25) with Eq. (27) we have $A_2^+ = A_2^- \exp(-i4yp)$, which then gets directly subtracted from the phase in Eq. (14), so integrating over $|y| \leq \beta/2^{1/2}$ and z gives

$$P^{II}(\Delta k L_c) = P_0^{II} \exp\left[-\left(\frac{\Delta k L_c}{2\beta}\right)^2\right] 2[1 + \text{sinc}(\Delta k L_c) \times \cos(\Delta k L_c + \phi_r)], \quad (29)$$

where $P_0^{II} = P_0^I (2\pi)^{1/2} / 2\beta$ (if the large β is due to tight focusing, one should include the correction factor from Subsection 3.D for quantitative accuracy). Equation (29) now has the same modulation frequency as case I, but the modulation amplitude is damped by the sinc function and the overall envelope is the much wider Gaussian. A comparison of the two cases is shown in Fig. 7. Because the sinc and the Gaussian are similar near $\Delta k = 0$, the form is nearly identical in the center region. Only the magnitude changes. Also shown is the single-pass case, demonstrating that although the single-pass SHG determines the width of the tuning curve, it remains one half to one fourth smaller than in the double-pass case. In fact, the ratio of the double-pass maximum to the single-pass maximum is plotted in Fig. 8 versus

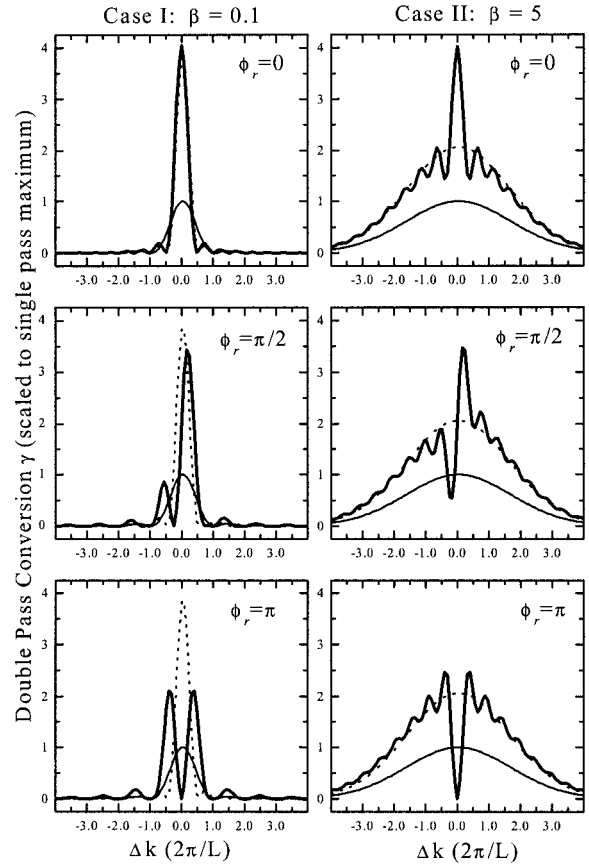


Fig. 7. Comparison of SH conversion double-pass tuning curves (solid curves) for case I ($\beta = 0.1$) and case II ($\beta = 5$) for three reflection phase shifts ($\phi_r = 0, \pi/2, \pi$). Each figure is normalized to the single-pass case of length L_c (dashed curve) and shown with the single-pass case of length $2L_c$ (dotted curve).

the reflection phase shift ϕ_r , which we can see is always greater than 2. The effect of the walk-off compensation is most evident when one compares the case II double-pass curve to the case of crystal length $2L_c$ also shown in Fig. 7. Clearly the backreflection does much more than just double the effective length of the crystal, because the double-pass maximum is a factor of 2 higher for $\phi_r = 0$.

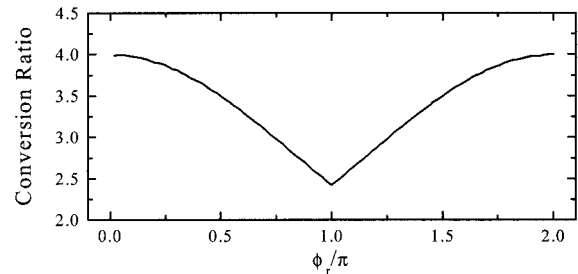


Fig. 8. Ratio of maximum double-pass SHG conversion to the single pass versus relative phase mismatch ϕ_r , caused by the HR crystal coating for $\beta = 2$.

D. Effects of Focusing

The small error shown in Fig. 6 between the semi-analytic result and the heuristic equation consists of an amplitude increase and a negative phase shift, both of which are results of our assumption of a constant beam diameter. This error can be significant when one is operating near optimum focusing parameter $L_c/2z_0 \gtrsim 1$, as many people do. We have ignored these focusing effects for simplicity and ease of interpretation, but we can easily correct for them for a more quantitatively precise result.

The phase shift comes from the Guoy phase lag of $\phi(x) \equiv \arctan(x/z_0)$ that a Gaussian beam passing through its waist sees relative to a plane wave. The application to SHG was discussed by Boyd and Kleinman.²² It is a linear shift near the waist, and for our purposes we can account for it by simply subtracting it from the relative phase such that $\Delta k \rightarrow \Delta k - \phi_f/L_c$, where $\phi_f = \arctan(L_c/z_0)$. It is important to note that to do so amounts to translating the horizontal axis ($\Delta k L_c$) of our power-tuning curves by this fixed offset. Therefore our not including this offset does not really affect our results. Even though it may look initially as if the new argument ($\Delta k L_c - \phi_f + \phi_r$) in Eqs. (28) and (29) would shift the interference pattern in Fig. 7 in a manner similar to ϕ_r , this shift is also in all the single-pass arguments, so the form of the tuning curve in fact remains the same in the end.

The amplitude error is dominated by an unaccounted-for intensity reduction as the beam expands away from the beam waist at the mirror. Because the SHG is highly sensitive to this reduction and the contribution of each small length of crystal is proportional to the inverse area of the fundamental beam, we can reduce the final power simply by a factor of the average squared waist:

$$\begin{aligned} \wp &= \left(\frac{w}{w_0} \right)^2 = \frac{z_0}{L_c} \int_0^{L_c/z_0} \frac{dx}{1+x^2} = \frac{z_0}{L_c} \arctan(L_c/z_0) \\ &= \frac{z_0}{L_c} \phi_f \end{aligned} \quad (30)$$

which clearly goes to unity for small focusing parameters.

We mention two final issues regarding focusing: First, if there are no other constraints on the cavity beam waist [thermal lensing, blue-light-induced infrared absorption (BLIIRA), optical damage limits, angular bandwidth], there is the question of choosing the optimum focusing parameter for the double-pass system. For a single pass this choice was dealt with thoroughly by Boyd and Kleinman,²² but for the double pass it may not be immediately clear: Does one optimize each single pass of length L_c , as would seem appropriate from Eq. (14), or optimize the double pass of length $2L_c$, as Fig. 5 would seem to suggest. It turns out that it makes no difference. The optimum waist calculated from Ref. 22 for length $2L_c$ with the waist at the center, or for L_c with the waist at the end

face, is the same, so one can just use the graph in Ref. 22 for length $2L_c$ and the waist at the center.

The second issue is that these calculations do not take into account the effect of angular bandwidth on a focused beam. If angular bandwidth $\delta\Phi$ (FWHM of the power-tuning curve) owing to the dependence of Δk on Φ is less than angular divergence $2\phi_0 = 2\lambda/(\pi n w_0)$ of the fundamental beam, then the phase-matching condition is not met for all Fourier components of the beam. This issue is addressed in several places for certain circumstances; usually a sort of weighted average is taken of the contributions of all Fourier components that compose the beam.^{28,29} We do not present any simple approximation or even estimation for this effect but simply point out that this condition exists both for our experiment and that of Bode *et al.*¹¹ and seems to be the most likely explanation for the lower-than-expected conversion efficiency.

4. Experiment

A. Cavity Details

Our need for more than 100 mW of power at the Sr resonance of 461 nm meant converting a strong, longer-wavelength pump laser through a dye or a nonlinear cavity. It was clear, because SHG cavities commonly achieve greater than 50% conversion, that we could get by with several hundred milliwatts of power at 922 nm, which could most cheaply and reliably be obtained from a semiconductor tapered amplifier. We used an SDL TD444 tapered amplifier whose gain spectrum at room temperature covered roughly 900–950 nm. We injected it with a grating stabilized diode master laser at 922 nm with two 35-dB optical isolators needed to prevent feedback from the input facet of the amplifier. For amplifier drive currents of 1–1.4 A, and injected powers of <1 to 13 mW, the amplifier output reached greater than 500 mW. The strongly astigmatic output was collimated with an $f = 8$ mm lens for one axis, followed by a cylindrical lens for the other axis. This beam passed through two more isolators and a telescope before being directed to the cavity. Despite the apparently square shape of the amplifier output, we typically coupled 80–85% of the remaining light into the TEM₀₀ mode of the cavity.

The actual cavity that we built was a little larger than indicated in Fig. 1 to accommodate temperature control, cavity alignment, and modulation. Our values for the surfaces shown in Fig. 1 are described as follows:

S1 is a 45° dichroic beam splitter with reflection coefficients $R = \text{HR}$ (922 nm) and $R = 7\%$ (461 nm).

S2 is a spherical mirror with a ROC of 35 mm and reflection coefficients $R = 96.7\%$ (922 nm) and $R = 4.7\%$ (461 nm).

S3 is a double AR-coated crystal surface with $R < 0.25\%$ (922 nm) and $R < 0.5\%$ (461 nm).

S4 is a double-HR-coated crystal surface with $R > 99.9\%$ (922 nm) and $R < 99.5\%$ (461 nm). Direct

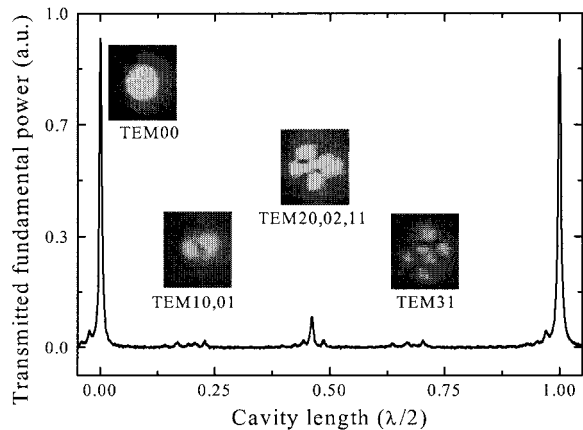


Fig. 9. Typical cavity scan of a slightly nondegenerate cavity, showing two TEM_{00} modes with the higher-order modes separated by roughly $FSR/4$.

transmission measurements indicate that $R > 99.9999\%$ at 922 nm.

From Eq. (4), the 35-mm ROC gives a confocal waist of $72 \mu\text{m}$, where for $\mathcal{R} = 0.5$, $L_a = 13 \text{ mm}$. We generally operated the cavity in a slightly nondegenerate mode with $0.5 < \mathcal{R} < 0.6$.

Figure 9 shows a typical sweep over one free spectral range of the cavity in which the transverse modes can be clearly seen to have the nearly $c/8L_p$ spacing that was described in Section 2. We chose a mode radius much larger than the optimum waist of $31 \mu\text{m}$ to try to avoid the power-limiting effects of thermal lensing and BLIIRA that was a concern of previous work,^{11,14,30–34} which we discuss in Subsection 4.C below. The shorter cavity and larger waist may also mean that the beam diameter at the mirrors can be smaller than in longer cavities, increasing the need for quality coatings that can hold up to higher intensities. Our first input coupler was found to have degraded during the first year of use.

Our KNbO_3 crystal is $10 \text{ mm} \times 3 \text{ mm} \times 3 \text{ mm}$ and is cut as indicated in Fig. 5, with the orientation specified at $\Phi = 48^\circ \pm 0.5^\circ$. The phase-matching temperature of $27.3^\circ \pm 1^\circ \text{C}$ at 921.7 nm indicates a cut of $48.56^\circ \pm 0.16^\circ$. This gives a walk-off of $\rho = 0.99^\circ$ and should produce a d_{eff} of approximately 18 pm/V . Though we were not able to measure this value directly, the unexpectedly low conversion described in Subsection 4.A may indicate a lower value for d_{eff} as a partial factor. It is well known that crystal quality can vary and that KNbO_3 can be damaged by thermal or mechanical stress. It could be that the daily temperature cycling that is done in initial operation of the cavity has caused the crystal to depole. It is recommended that one vary the temperature more slowly than 0.5°C/min (Ref. 35) to prevent this degradation or, better yet, keep the crystal at one temperature continuously.

To minimize the chance of sudden temperature changes, we maintained the entire cavity on an en-

closed, heated base held near the phase-matching temperature. The large thermal mass ensured that failure of the temperature control system would not permit a sudden drop in the crystal's temperature. Fine control of the crystal's temperature was done with a small Peltier cooler underneath the Cu crystal mount. The crystal was held in place by spring-loaded Cu foil on the top and one side that pushed gently into a square corner to give it thermal contact on all sides while still preventing stress from thermal expansion. A thermally conductive pad surrounded the crystal for better contact, providing a time constant of the order of a second.

Although it is possible to operate at 922 nm with noncritical phase matching, a crystal temperature of 150°C is required. We chose to work at room temperature, which has several advantages:

- First, it is technically much easier to design, construct, maintain, and use a cavity at room temperature. Because of the compact size of our cavity, we would otherwise be required to maintain the entire apparatus at the same high temperature as the crystal.
- Second, 150°C is very near the phase transition temperature of 180°C , and thus is less stable against depoling.
- Finally, as we discuss in Subsection 4.C below, the thermal effects that can limit SHG can be much reduced at room temperature. A ring cavity operating at 150°C was unstable for $P_{2\omega} > 180 \text{ mW}$ because of thermal problems.³⁶

Under the Peltier cooler was a five-axis NewFocus stage that facilitated angular alignment of the cavity as well as three-axis control of the crystal position to permit the use of different parts of the crystal or of the coating if there were defects, without misaligning the cavity. The input coupler was mounted onto a Piezo Mechanik 500 V piezoelectric stack tube offering nominally $5 \mu\text{m}$ of translation along the axis. This coupler was screwed into an Al mount that held the dichroic beam splitter such that both could easily be removed or replaced. An amplified photodiode was mounted behind the crystal for monitoring of the transmission signal, though care had to be taken because both the fundamental and the SH could contribute to the signal.

Stabilization of the cavity resonance to the fundamental frequency could be accomplished either by use of the fundamental wavelength transmitted or, for operation at high enough powers, of the SH output. We found the latter to work well for daily use (especially if the problem in transmission mentioned above is considered), allowing us to lock to the maximum of the blue output. We used a modulation of 20 kHz on the piezo mirror, which we detected on a small SH signal transmitted through a dielectric mirror following the dichroic beam splitter.

With the cavity, and hence within the SH, we used the output slaved to the master laser to provide a saturated-absorption signal from a Sr heat pipe,

which was then used to stabilize the master laser to the $5^1S_0-5^1P_1$ transition. The saturated-absorption error signal from the counterpropagating pump-probe pair was again obtained through a modulation, this time at 30 kHz, introduced by an acousto-optic modulator to the pump beam. The heat pipe was made from standard C25 ultrahigh-vacuum tubing roughly 20 cm long with a sapphire conflate window on either end and a 5-cm-long section of heating coil welded to the center. A vacuum cross was added to one end for a gauge and a pumping port. It was loaded with Sr in an Ar atmosphere, then pumped down to vacuum, reloaded with approximately 100 kPa of Ar, and sealed. By varying the temperature near 300 °C we obtained a well-controlled absorption, such that the cell could go from almost transparent to nearly opaque. The Ar collision rate is high enough to act as a buffer, ensuring that the Sr vapor reached a cold section of the pipe before reaching a window but low enough to ensure that the collisional broadening and frequency shift were well within the transition linewidth. Based on the noise in the error signal of the cavity feedback loop, we put an upper bound of 2 MHz on the laser linewidth. The result was a stable, tunable or frequency-stabilized output that supplied sufficient power for both the Zeeman slower and the MOT described by Bidet *et al.*³

B. Blue-Light-Induced Infrared Absorption

BLIIRA is generally regarded as the limiting factor in SHG to the blue wavelengths with KNbO₃. Although the precise mechanisms are uncertain, the most popular model suggests that the presence of blue light depopulates low-level traps through photoionization, which then allows for increased infrared absorption.³⁰ We can then describe the total power (blue and IR) absorbed P_{abs} in the crystal for blue and IR linear absorption coefficients $\alpha_{2\omega}$ and α_ω by

$$P_{\text{abs}} = [\alpha_\omega P_c + \alpha_{2\omega} P_{2\omega} + \alpha_b(I_{2\omega}) P_c] 2L_c. \quad (31)$$

This additional, blue-intensity-dependent IR absorption [$\alpha_b(I_{2\omega})$] is often considered to explain the deviation from the theoretical SHG efficiency curves at higher powers.^{11,33,36} Although the time scales and effects can be similar to those that one might expect from thermal problems through simple absorption, BLIIRA combined with the thermal sensitivity of KNbO₃ can cause complicated and dramatic effects.³² Some focused quantitative studies have been done to characterize both linear absorption and BLIIRA as a function of wavelength, temperature, doping, and power.^{30,32,34} One can summarize these as follows:

- Parameters vary greatly from crystal to crystal.
- Undoped crystals tend to have higher absorption in the IR but lower absorption in the blue and less temperature dependence for BLIIRA.
- Higher temperatures reduce absorption greatly in doped crystals and slightly in undoped crystals.

- Undoped KNbO₃ tends to have very low α_ω , in the range 0.05–0.3% cm⁻¹, and very high wavelength-dependent $\alpha_{2\omega}$, in the range 2–10% cm⁻¹.
- Undoped KNbO₃ seems to have a BLIIRA threshold near 5 kW cm⁻², above which it becomes linear in $I_{2\omega}$ with a slope of 2–300 cm MW⁻¹ (increasing inversely to blue wavelength), and below which it goes as $\log(I_{2\omega})$ with a maximum of approximately 0.3–0.5% cm⁻¹.

The last point seems consistent with published results, which generally show the deviation from non-BLIIRA theory near this 5-kW cm⁻² value, above which the absorption can reach several percent per centimeter. Below this value one can expect BLIIRA to be roughly 2–3 times the linear IR absorption, and therefore, without precise measurements, it could easily be mistaken for larger passive cavity losses and larger conversion factors.

The BLIIRA, even when it is small relative to the conversion factor, can still reduce efficiency, as shown in Fig. 4, and this will be even more dramatic above the threshold. Because the absorption can vary significantly one must take care in increasing the crystal length or reducing the beam waist to increase γ because both of these changes are likely to increase the total loss. For example, we can see that $\gamma \propto L_c/w_0$. If we write the loss as a fixed loss plus absorption, $\mathcal{L} = \mathcal{L}_0 + \alpha_\omega L_c$, then Eq. (6) will show that when $\alpha_\omega L_c > \mathcal{L}_0$ the efficiency will start to decrease with increasing L_c . This condition is quite possible with BLIIRA and a low loss semimonolithic cavity.

To reduce BLIIRA effects we chose our waist to be 72 μm , such that we would expect a maximum blue intensity to be well below 5 kW cm⁻² (assuming ~ 300 mW of blue), and still predicting a power-conversion factor of greater than 10^{-3} (assuming that $P_{\text{in}} = 400$ mW and $\gamma = 8 \text{ kW}^{-1}$ calculated for our parameters with $d_{\text{eff}} = 18 \text{ pm/V}$ and worst case $\phi_r = \pi$). Except by selecting larger beam waists, and perhaps operating at a higher temperature, one may be unable to avoid BLIIRA.

C. Thermal Effects

The detrimental effects of BLIIRA can go well beyond that of simply increasing the losses as described above. Increased absorption at large intracavity intensities can cause significant transverse and longitudinal thermal gradients inside the crystal, which can lead to reduced mode matching or mode quality as a result of thermal lensing,^{14,31} variation in phase mismatch caused by longitudinal gradients,³² or even cavity instability.³⁶ Sorting out which effects are present can be difficult, but some values can easily be estimated with some simple models.

Similarly to Polzik and Kimble,³¹ we can analyze this cavity, deriving equations that describe the steady-state thermal gradients in the crystal by approximating the crystal as an infinite cylinder of radius a and solving the heat diffusion equation assuming a constant heat source from the beam absorption at the center. Although we do include

the SH absorption in the heat source, we simply consider that all the power is confined in a Gaussian beam of fixed waist w_0 . Temperature $T(a)$ at the crystal boundary is fixed by a stabilized feedback loop, which results in the following temperature-difference profile:

$$T(r) - T(a) = \Delta T \left[1 - \frac{\mathcal{F}(r)}{\mathcal{F}(a)} \right], \quad (32)$$

$$\begin{aligned} \mathcal{F}(r) &= \gamma_E + \ln(\tilde{r}) + \int_{\tilde{r}}^{\infty} \frac{\exp(-t)}{t} dt \\ &= - \sum_{t=1}^{\infty} \frac{(-\tilde{r})^t}{t!t} \sim \tilde{r}, \end{aligned} \quad (33)$$

$$\tilde{r} \equiv 2 \left(\frac{r}{w_0} \right)^2, \quad (34)$$

$$\Delta T \equiv T(0) - T(a) = \frac{P_{\text{abs}} \mathcal{F}(a)}{4\pi L_c k_{\text{th}}}, \quad (35)$$

where $k_{\text{th}} = 0.4 \text{ W cm}^{-1} \text{ K}^{-1}$ is the thermal conductivity of undoped KNbO_3 (Ref. 32) and $\gamma_E = 0.577215 \dots$ is Euler's constant.

Obviously the most important parameter for thermal effects is temperature dependence of the index of refraction, where fundamental index n_1 is relevant for thermal lensing and difference $n_1 - n_2$ is relevant for the thermally induced phase mismatch. We denote the dependence on temperature of n_1 by $\dot{n}_T = \partial n_1 / \partial T$ and the phase-mismatch dependence by $\Delta \dot{k}_T = \partial \Delta k / \partial T$. These dependencies are calculated and graphed in Appendix A for various fundamental wavelengths and temperatures. We can see that for our parameters the calculated values of $\Delta \dot{k}_T = -15 \text{ cm}^{-1} \text{ K}^{-1}$ and $\dot{n}_T = 6 \times 10^{-7} \text{ K}^{-1}$ are factors of 2 and 50 times smaller, respectively, than those expected at $150 \text{ }^\circ\text{C}$ by Vogel,³⁶ for which thermal problems were seen. One can see that for the 50 nm from 920 to 970 nm one can choose the temperature for critical phase matching at which $\dot{n}_T = 0$. Although $\Delta \dot{k}_T$ increases with temperature for a given wavelength, we shall see that this increase will be less critical in our configuration because both the fundamental (because of its larger waist) and the SH (because of its symmetric reflection) beams are longitudinally distributed nearly evenly through the crystal, thus greatly reducing the phase-mismatch gradient problems discussed by Busse *et al.*³²

One can compensate for uniform longitudinal heating during continuous wave operation by adjusting the temperature set point for maximum SHG after the cavity is locked to the resonance. Comparison of the difference between the optimum set temperatures of low average power operation (continuous wave at low input powers or pulsed operation) and those at high average power operation can be used to approximate a measured ΔT value for Eq. (32). For our measurements we found ΔT values as high as $1.4 \text{ }^\circ\text{C}$. This value can also be estimated for compar-

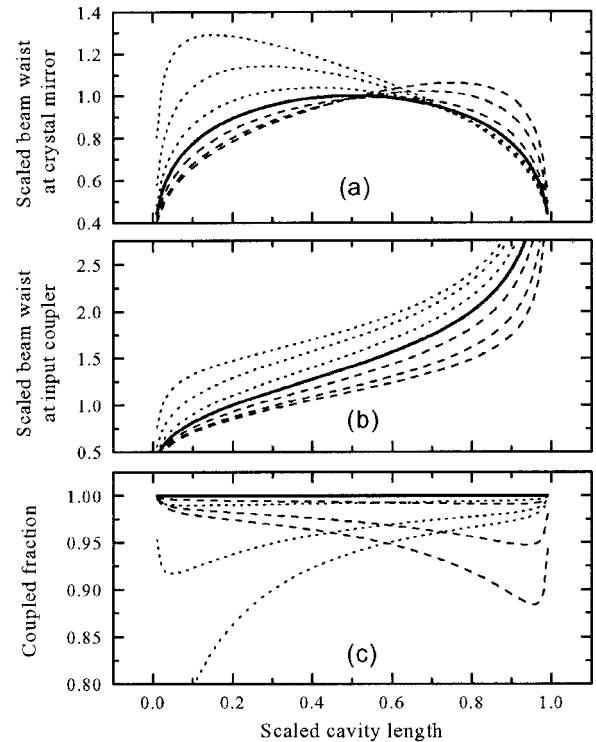


Fig. 10. Effect of thermal lensing on (a) the waist in the crystal, (b) the beam radius at the input coupler, and (c) the fraction of the cold-cavity mode that will still couple to the thermally altered modes versus scaled cavity length for various thermal index gradients \hat{n} . Solid curves, the cold cavity ($\hat{n} = 0$) case shown in Fig. 3. Dashed (dotted) curves, positive (negative) thermal index gradients of values $\hat{n} = +(-)0.1, +(-)0.2$, and $+(-)0.25 \text{ cm}^{-2}$ moving out from the solid curves.

ison by use of Eq. (32) and expected values for $\alpha_\omega, \alpha_{2\omega}, \alpha_b, P_{2\omega}$, and P_c . Assuming typical values of 0.2%, 5%, and $0.5\% \text{ cm}^{-1}$ and of 180 mW and 6 W, respectively, we get $\Delta T = 1.5 \text{ }^\circ\text{C}$.

To evaluate the significance of thermal lensing with the *ABCD* matrix formalism, we approximate the induced transverse index profile with a quadratic index profile, using the approximation for $T(r)$ given by relation (33) (Refs. 27 and 31):

$$n(r) = n(a) + \dot{n}_T [T(r) - T(a)] \quad (36)$$

$$= n(a) + \dot{n}_T \Delta T - \frac{2\dot{n}_T \Delta T}{\Gamma(a)w_0^2} r^2 \quad (37)$$

$$= n(0) - \frac{\hat{n}}{2} r^2, \quad (38)$$

$$\hat{n} = \frac{4\dot{n}_T \Delta T}{\mathcal{F}(a)w_0^2}. \quad (39)$$

Figure 10 shows, for our input coupler, the effect that heating of the crystal will have on the mode, and hence on input coupling and SHG efficiency, versus the scaled cavity length, defined as in Section 2 for various values of \hat{n} . The solid curves show the unperturbed cavity as in Fig. 3, with the variations that

are due to positive (negative) index gradients shown by the dashed (dotted) curves. The quadratic index profile is of course a rough approximation, but this figure shows us, first, that for both positive and negative thermal index gradients there are cavity lengths just slightly greater than the confocal length that can minimize the effect of thermal lensing on the waist in the crystal, thus giving stability to the SHG process. Second, we can see that the beam radius error at the input mirror increases in proportion to the index gradient for all cavity lengths, meaning that some error in mode matching is inevitable. The mode-matching fraction still remains above 90% near the confocal region, even for the largest perturbations shown. Although cavities with smaller waists are less sensitive to \dot{n} , the w_0^{-2} dependence overcomes this advantage, making the overall effect more pronounced.

For our parameters, $\dot{n} \sim 10^{-2} \text{ cm}^{-2}$ is an order of magnitude smaller than the values shown, so we expect no effect from thermal lensing. Recall that this is so largely because we are working near the zero of the \dot{n}_T curve. In general one should consider carefully the cavity length for compensation. Another effect to consider is that of longitudinal gradients caused by the longitudinal buildup of blue power (contributing both directly through $\alpha_{2\omega}$ and indirectly by BLIIRA) and by the natural diffraction of the beam. We can largely resolve the diffraction problem by working in the weak-focusing regime, but in addition the $ABCD$ analysis shows that this effect can be reduced further for small, positive index gradients, as thermal lensing counteracts the beam diffraction. Although our $ABCD$ calculation supposes constant \dot{n} values for each curve, self-consistent calculations made elsewhere have shown little difference.³¹ For the blue power buildup, the retroreflection in the crystal ensures that the SH intensity will change by less than a factor of 2 along the length of the crystal, which is much more nearly uniform than single-pass systems.

D. Results

As stated in Section 1, the output of the SHG is unusual. It will in general show neither the $\text{sinc}^2[\Delta k(T)L_c]$ temperature dependence in the power that one typically associates with plane-wave SHG nor the Gaussian or elongated Gaussian intensity profile that one sees in single-crystal unidirectional SHG. Instead, one sees in the temperature-tuning curve the complex modulation described in Subsection 3.C that is uniquely characteristic of the situation reflected in Fig. 5 and the associated lobed forms in the output intensity profiles as shown in Fig. 11. Indeed, one can even use the tuning curve to measure the reflection phase shift. In this section we compare our experimentally measured tuning curve and beam form dependence, for the parameters given above, with that predicted in Section 3 for both the analytic equation and the numerical integration.

Figure 12 shows the measured SH output (diamonds), as we varied the temperature of the crystal

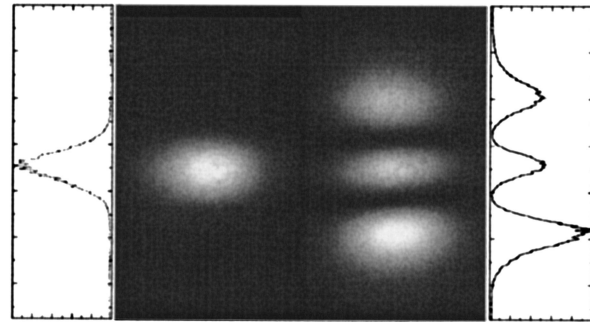


Fig. 11. Example of CCD images of the SH far-field intensity profile along with curves that show the y axis cut through the center for $\Delta kL_c/2\pi \sim 1.72$ (right) and for the maximum at $\Delta kL_c/2\pi \sim 0.47$ (left).

from 24.4 to 29.2 °C, overlaid on the theoretical curves that correspond to Eq. (20) (dotted curve) and to the numerical integration (solid curve) for a measured coupled input power of 10.7 mW, corresponding to a circulating power P_c of 750 mW (assuming a cavity buildup of approximately 70, based on finesse measurements). This low power allows us to minimize thermal effects and to make a simple comparison to the theoretical curves by assuming a constant circulating power related to the input by the low-power cavity finesse. This is so because at small powers the cavity finesse is dominated by the constant parasitic loss and thus the SH output is just proportional to γ by $P_2 = \gamma P_1^2$. The temperature was measured with a digital thermometer with a type-K thermocouple to be accurate to less than 1 °C. The horizontal axis is given both in temperature and in units of $\Delta k(T)L_c/\pi$ as calculated in Appendix A,

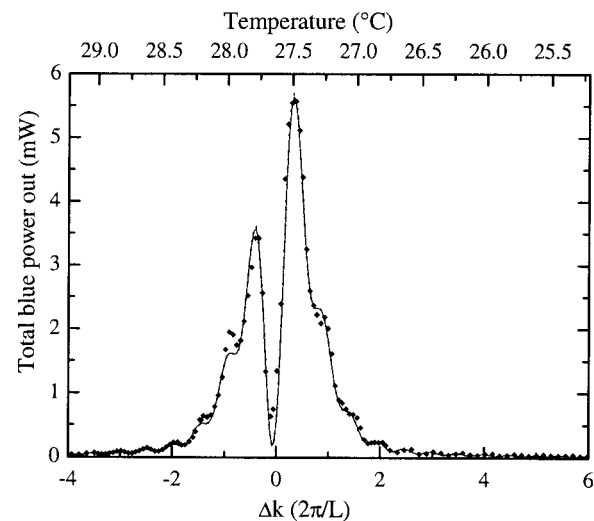


Fig. 12. Comparison of temperature-tuning curve $P[\Delta k(T)L_c]$ for the adjusted experimental data (diamonds), the analytic equation (solid curve), and the nearly indistinguishable numerical integration (dashed curve). Upper and lower axes, measured temperature and associated phase mismatch, respectively, as related in Appendix A. Data are multiplied by 6 to permit a qualitative comparison with the calculations.

with the $\Delta k = 0$ point left as an adjustable parameter with which to align the data horizontally with the theoretical curve. For the calculations we use values of $d = 18$ pm/V and $\phi_r = 0.75\pi$; the latter is chosen by eye to give the best fit. Although these parameters predict a factor-of-6 more SH power, we attribute this discrepancy largely to the effects of the small angular bandwidth and perhaps to a smaller value of d because d was not measured. Our beam divergence of $2\phi_0 = 3.68$ mrad is significantly larger than the Φ angular bandwidth $\delta\Phi = 1.04$ mrad but smaller than the Θ angular bandwidth, $\delta\Theta = 23.2$ mrad. Nonetheless, by scaling the data in Fig. 12 we can see that the complex structure in the temperature-tuning curve is well described by this simple analysis.

We additionally made at each temperature a CCD image of the output beam illuminating a spinning paper card at a distance of 90 cm from the cavity entrance. Two examples of such CCD images are shown in Fig. 11, with the corresponding intensity slices shown above and below. The left-hand image was taken at the peak of the tuning curve. The ratio of the y and z widths is $\sim 2/5$, which is actually less elliptical than a single pass would be. Recalling that this is the far field, one would expect the visible ellipticity in the left-hand spot to be opposite the walk-off direction and hence opposite the y -axis modulation (shown vertical in these images).

A similar slice was taken at each temperature to show the modulation of the y -axis beam profile as a function of Δk . The experimental slices are shown in Fig. 13(a) below the corresponding calculated profiles. Each slice was normalized by its maximum intensity to show the structure better, as the power dependence versus Δk was already shown in Fig. 12. We can see that the semianalytic Fig. 13(b) and the full numerical integration Fig. 13(c) are almost indistinguishable and that both reproduce the experimental beam profiles, though again discrepancies may be expected because of the angular bandwidth problem.

Finally, in Fig. 14(a) we present the measured efficiency versus input power, which shows as much as 75% efficiency, along with the associated reflection data in Fig. 14(b). These data were taken with a spatial filter in place, reducing the maximum power available to 180 mW while only slightly improving the mode-matching efficiency. For the measured points (diamonds), 85% mode matching of the measured input power and a 14.65% loss of the blue power are assumed. The blue loss includes the input coupler (5%) and the dichroic beam splitter (7%) and assumes the lowest absorption (1.5%/cm) reported by Busse *et al.*³² Higher absorption or inclusion of small losses at HR- and AR-coated surfaces would indicate even better efficiency. Comparing Fig. 14 with Fig. 4 suggests losses of less than 1% in the IR. For the solid curve presented for comparison we suppose that $\gamma = 4.0$ kW⁻¹, $\mathcal{L} = 0.2\%$ cm⁻¹, and $\alpha_b = 0.13\%$ cm⁻¹ at the maximum. The dotted curve is for no BLIIRA and with $\gamma = 4.6$ kW⁻¹.

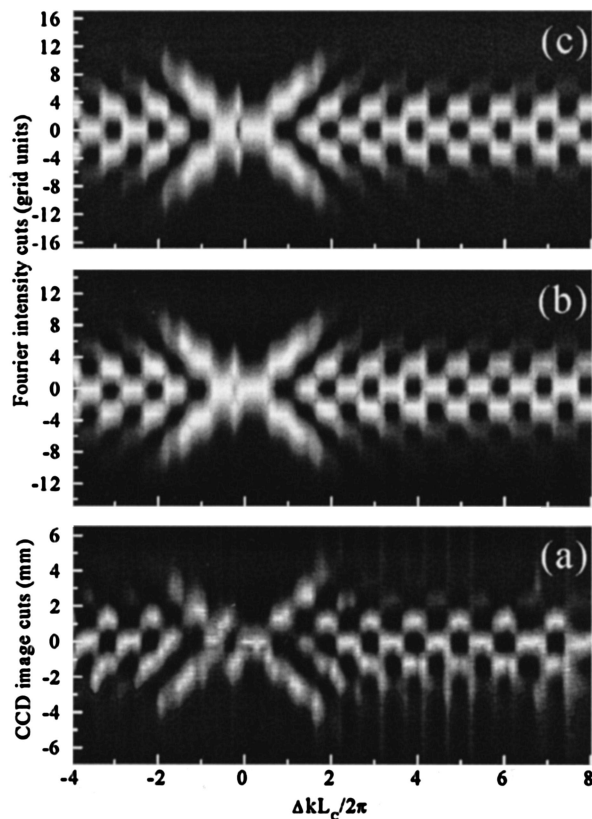


Fig. 13. Comparison of (a) the y -axis modulation of SH intensity profiles measured by a CCD camera in the far field with the profiles predicted by (b) Eq. (14) and by (c) numerical integration of Eqs. (11) and (12) as we vary Δk . The camera image plane is ~ 90 cm from the waist in the crystal, and profiles in (b) and (c) were obtained from the Fourier transform of the near-field calculations.

These values have not been precisely measured: The curves are simply intended to show qualitative agreement for reasonable values. We can see that although both curves match equally well in reflection, the BLIIRA makes a big difference in lowering the efficiency. In this regime, $\gamma P_{\text{in}} \sim 0.5 \times 10^{-3}$, we would gain some efficiency by shortening the crystal to reduce the overall loss and increase the angular bandwidth. This is especially true when more input power is available. We have achieved as much as 200 mW of internal SH power at 461 nm for a raw input of 404 mW of IR radiation and no spatial filter. This shows reduced efficiency ($\eta \approx 58\%$, assuming that $\epsilon = 0.85$) despite the higher powers. We have not considered resonant effects caused by the 5% reflection of the SH light, which could increase the BLIIRA slightly owing to enhanced internal SH intensity, but we have not noticed any problem in maintaining stable operation.

5. Conclusions

We have presented an analysis of a semimonolithic standing wave cavity for second-harmonic generation, considering the effects of this configuration on design, tuning, thermal effects, and optimization. We have attempted to present this analysis in a prac-

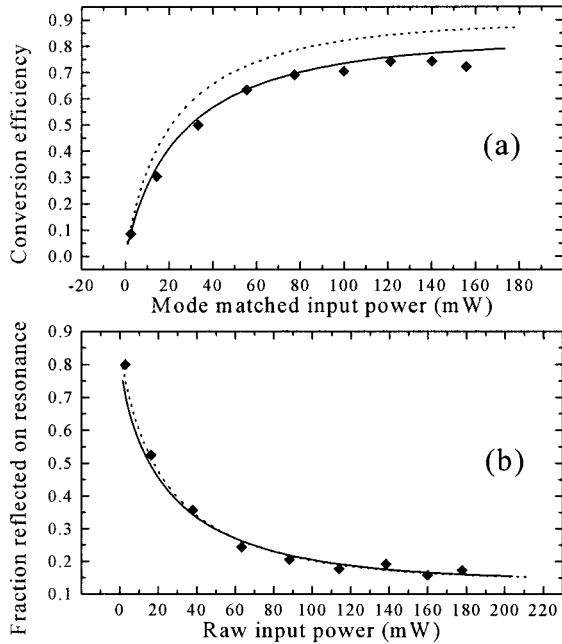


Fig. 14. Experimental data (diamonds) for (a) conversion efficiency $\eta = P_{2\omega}/P_{in}$ versus mode-matched power P_{in} and (b) the experimental reflected power ratio (on resonance to off resonance) versus total power in P_{in}/ϵ . Shown for comparison are curves calculated with (solid curves, see text) and without (dotted curves) BLIIRA.

tical manner to aid any researcher in need of such a device to build and understand it. The advantages of this standing wave cavity relative to a traditional ring cavity center about its compact monolithic construction, which reduces cost and loss while it enhances stability and simplicity, and its single-output standing wave design, which offers automatically aligned walk-off compensation and reduced longitudinal intensity gradients. Additionally, the on-axis design is coma free and allows one to easily vary the input mode diameter by more than a factor of 2 with little effect on the SHG. We have shown a SHG efficiency of $>70\%$ at input powers of 120 mW, whereas other researchers, who used a shorter crystal (less loss), achieved 81% efficiency at ~ 340 mW input, despite the fact that in neither case was the HR coating phase shift on the crystal optimized (in fact, our phase shift was nearly a worst case).

We have focused primarily KNbO_3 because of its wide range of compatibility for SHG, its large nonlinear coefficient, and its adaptability to critical or noncritical phase matching. Although we have emphasized and demonstrated its advantages as a tunable, high power source that is suitable for laser cooling and atomic spectroscopy in the blue-green spectral region, it should work even better at longer wavelengths, where BLIIRA will not be a problem, a fact that becomes increasingly more interesting as more solid-state sources develop in the 1.1–1.4 μm range, where for KNbO_3 the walk-off is 2° – 4° .³⁷ When they are combined with efficient SHG these sources could provide convenient sources for trapping

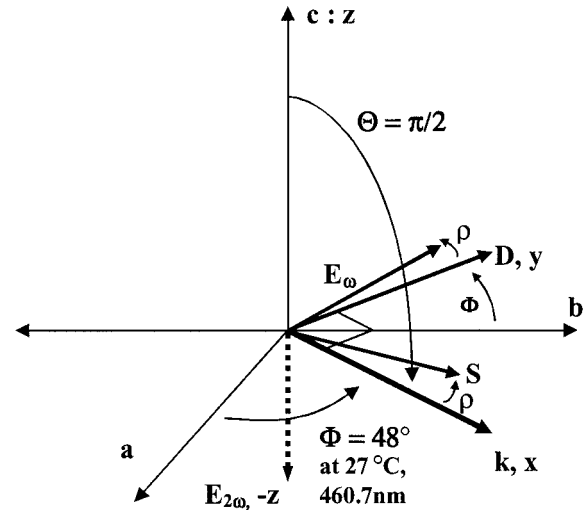


Fig. 15. Depiction of axis definition for relating crystallographic axes (a, b, c) to lab axes (x, y, z) defined by the chosen polarization (y) and propagation (x) directions. This example is appropriate for KNbO_3 of type I ($e + e = o$) phase matching described in the text. Here Φ is the phase-matching angle in the a - b plane, ρ is the walk-off angle, \mathbf{S} is the Poynting vector, \mathbf{k} is the wave vector, \mathbf{D} is the displacement vector, and \mathbf{E}_ω and $\mathbf{E}_{2\omega}$ are the fundamental and the SH electric field vectors, respectively. All vectors are in the a - b plane, except for $\mathbf{E}_{2\omega}$, which lies along the $-z$ axis.

or spectroscopy in the red–yellow region (for example, for lithium or sodium).

The principal advantages of this crystal can be applied to other crystals as well. Retroreflecting SHG with a separate reflecting mirror has even been done with periodically poled structures, for which walk-off is not a problem.^{25,38} Juwiler *et al.*²⁵ showed that wedge structuring can control the reflection phase mismatch, which, by this analysis, could mean that higher efficiencies would be achieved with shorter crystal lengths. Although Juwiler *et al.* suggested putting an input coupler on the crystal, we calculate that it would also be possible to use the wedged facet as the high reflector, thus combining this phase control in exactly the cavity form that we have been discussing.

Appendix A. Calculation of Constants

We wish to be able to calculate the crystal parameters used in this paper as functions of wavelength, temperature, and polarization. The starting point is necessarily index of refraction $\tilde{n}_j(\lambda, T)$, where $j \in \{a, b, c\}$ is one of the three crystallographic axes as defined by Biaggio *et al.*³⁵ and shown in Fig. 15. For any chosen propagation direction given by unit vector \mathbf{k} there are two possible polarization directions in the perpendicular plane (axes y and z in Fig. 15) for displacement vector \mathbf{D} on which the polarization propagates unchanged. Once we have the appropriate direction we can get the phase-matching angles and nonlinear coefficients used in Section 3 and the temperature derivatives used in Section 4 for any case. For a thorough explanation of such calculations and complete figures one should see Zysset *et al.*³⁹ and Biaggio *et al.*³⁵; however, to provide a stand-alone

Table 1. Sellmeier Coefficients for KNbO₃^a

<i>ij</i>	Coefficient				
	<i>S</i> 1 _{<i>ij</i>} (μm ⁻²)	<i>S</i> 2 _{<i>ij</i>} (μm ⁻²)	λ1 _{<i>ij</i>} (nm)	λ2 _{<i>ij</i>} (nm)	<i>D</i> _{<i>ij</i>} (×10 ¹⁰ m ⁻²)
1 <i>a</i>	20.05519	149.8408	258.157447	129.092177	2.517432
2 <i>a</i>	20.27475	152.338	258.664256	127.592234	2.514857
3 <i>a</i>	19.33691	150.4971	260.77236	129.504923	2.514893
4 <i>a</i>	16.60832	142.0508	265.628822	137.103137	2.51586
5 <i>a</i>	16.04692	140.7942	267.779572	137.395507	2.508202
6 <i>a</i>	13.89662	137.2157	273.698261	143.185689	2.511282
1 <i>b</i>	19.37347	135.4992	272.74569	137.003919	2.845018
2 <i>b</i>	20.6625	144.1607	271.398899	130.593449	2.827127
3 <i>b</i>	20.06891	142.7868	272.5307	131.949874	2.80751
4 <i>b</i>	14.37713	123.3481	281.956034	151.431231	2.79633
5 <i>b</i>	18.87445	138.8675	274.864168	135.282114	2.771253
6 <i>b</i>	22.1202	162.8852	271.016254	119.793115	2.762299
1 <i>c</i>	16.0917	165.4431	255.227833	119.71423	1.943289
2 <i>c</i>	18.24447	181.1303	252.752642	111.742295	1.945428
3 <i>c</i>	17.56954	176.6712	254.675941	113.973036	1.95288
4 <i>c</i>	14.0194	158.4156	262.219822	125.100075	1.968455
5 <i>c</i>	16.48284	167.7579	258.712779	118.491217	1.982648
6 <i>c</i>	21.47866	215.6493	252.773409	98.801194	2.004523

^aRef. 39. *T*_{*i=1, 2, 3, 4, 5, 6*} = 22°, 50°, 75°, 100°, 140°, 180 °C, respectively.

reference for reproducing this cavity with KNbO₃ at other temperatures and wavelengths we have organized the necessary equations and material coefficients in compact form in this appendix.

1. Index

Zysset *et al.*³⁹ provided an excellent analyses of the refractive indices of KNbO₃ and of the way to calculate $\tilde{n}_j(\lambda, T)$. We summarize the calculation:

1. One uses the Sellmeier equation [Eq. (A1)] to model the wavelength dependence of *n* at a given temperature, given the Sellmeier coefficients for that temperature. Zysset *et al.*³⁹ measured the five coefficients (*S*1_{*ij*}, *S*2_{*ij*}, λ1_{*ij*}, λ2_{*ij*}, *D*_{*ij*}) for six temperatures *T*_{*i*} (*i* = 1 . . . 6) on each axis, thus providing for each axis *j*

$$n_j(\lambda, T_i)^2 = [S1_{ij}(\lambda^2\lambda1_{ij}^2/\lambda^2 - \lambda1_{ij}^2) + S2_{ij}(\lambda^2\lambda2_{ij}^2/\lambda^2 - \lambda2_{ij}^2) - D_{ij}\lambda^2 + 1] \tag{A1}$$

for six measured temperatures. The coefficients and associated temperatures are provided in Table 1.

2. Next one assumes a quadratic dependence on temperature for a given wavelength of the form

$$n_j(\lambda, T) = C0_j(\lambda) + C1_j(\lambda)T + C2_j(\lambda)T^2. \tag{A2}$$

Given the six data pairs {*T*_{*i*}, $\tilde{n}_j(\lambda, T_i)$ } from Eq. (A1) for each axis, one can fit the quadratic equation for any desired wavelength. The results are accurate to ±1.5 × 10⁻⁴.

With these functions, one can calculate the needed crystal properties: walk-off angles; critical and non-critical phase-matching angles and temperatures for any wavelength; thermal lensing effects; and Δ*k* ver-

sus angle, temperature, or wavelength for finding tuning bandwidths. A direct application of these functions lies in finding the noncritical phase-matching temperatures for various wavelengths when *n*_{*c*}(2ω) = *n*_{*b*}(ω) or *n*_{*c*}(2ω) = *n*_{*a*}(ω).

2. Walk-Off

Solving Maxwell’s equations for the propagation of a plane wave in an anisotropic medium with dielectric tensor ε_{*ij*}, we find that

$$\mathbf{D} = \epsilon_0 n^2 \mathbf{E} - \epsilon_0 n^2 (\hat{\mathbf{k}} \cdot \mathbf{E}) \hat{\mathbf{k}}. \tag{A3}$$

As the Poynting vector is by definition perpendicular to **E**, and **D** is perpendicular to **k** by Eq. (A3), we can see that the walk-off results from the second term on the right-hand side of Eq. (A3). Its value can be obtained by inspection of Fig. 15 and the relation **D** = ε**E** once we get ε. By taking the dot product of Eq. (A3) with **D** and choosing the crystallographic basis, we can connect $\hat{\mathbf{n}}$ with the diagonalized dielectric tensor by ε_{*jj*} = ε₀ \tilde{n}_j^2 . Then from Fig. 15 we can see that, in terms of \tilde{n}_a , \tilde{n}_b , and Θ, the walk-off is given by

$$\rho = \arctan \left[\frac{\tilde{n}_b}{\tilde{n}_a} \tan(\Theta) \right] - \Theta. \tag{A4}$$

From Eq. (A4) it is clear that the propagation will walk off in the direction of the larger index, as shown in Fig. 15.

3. Effective Index and Phase Matching

For critical phase matching, for which we use the crystal birefringence to match the indices of the fundamental and SH waves, we need to calculate an effective index in the *y-z* plane from $\hat{\mathbf{n}}$. Equation (A3) readily gives the equation for an index ellipsoid formed by use of \tilde{n}_j^2 as the major axes of three-

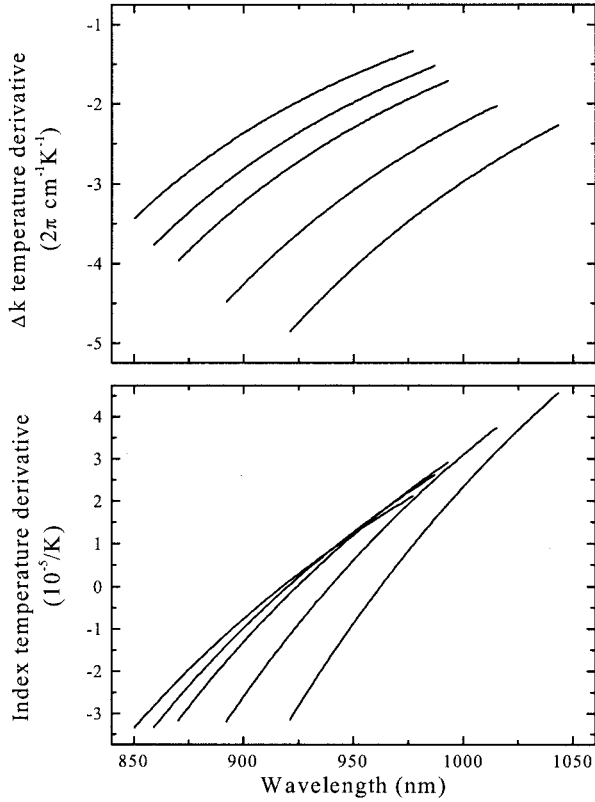


Fig. 16. Temperature dependencies of (top) the phase mismatch $(1/2\pi)\partial\Delta k/\partial T$ and (bottom) the effective index of refraction $\partial n_y/\partial T$ on wavelength for five temperatures, $T = 0^\circ, 27^\circ, 50^\circ, 100^\circ, 150^\circ \text{ C}$ (left to right). Each point was calculated for the phase-matching angle for that temperature and wavelength.

dimensional ellipsoid. From this equation one can deduce geometrically the formula for n in any given direction that, for propagation in a principal plane such as in Fig. 15, gives a simple ellipse such as

$$\frac{n_y^2 \sin^2(\Theta)}{\tilde{n}_a^2} + \frac{n_y^2 \cos^2(\Theta)}{\tilde{n}_b^2} = 1. \quad (\text{A5})$$

For phase matching we want $n_c(\lambda/2) = n_y(\lambda)$, which we substitute into Eq. (A5) to solve for Θ . Alternatively, we can rewrite Eq. (A3) as $\{\tilde{n}_i^2\} \mathbf{D} = n^2(1 - \mathbf{K})\mathbf{D}$, where $K_{i,j} \equiv \hat{\mathbf{k}}_i \hat{\mathbf{k}}_j$ and $\{\tilde{n}_i^2\}$ is a diagonal matrix, and solve it more generally for D_y, D_z, n_y , and n_z for a given λ and T .

Now we can numerically calculate the derivatives at any point as well, which can then be used for evaluating thermal effects as in Subsection 4.C. Figure 16 shows the temperature gradients of Δk and n_y versus wavelength for five temperatures; each point was calculated for the appropriate phase-matching angle. The wavelength range for each curve represents the phase-matching range for that temperature in this configuration.

4. Effective Nonlinear Coefficient

Coupled-wave equations Eqs. (11) and (12) are derived from vector equations: one for each polarization-frequency pair involved $(\hat{\mathbf{a}}, \omega)$. We want

to eliminate the tensor nature of each equation by defining a scalar d_{eff} that accounts for the configuration geometry. If we write each field as a complex scalar amplitude times a unit polarization direction $A_m \hat{\mathbf{a}}_m$, we can make each associated nonlinear polarization component $\hat{\mathbf{a}}_m \cdot \mathbf{P}(\omega) = \epsilon_0 [\hat{a}_m]_i d_{ijk} [A_{m'}]_j [A_{m''}]_k$ into a product of scalars by the definition

$$\begin{aligned} [\hat{a}_m]_i d_{ijk} [A_{m'}]_j [A_{m''}]_k &= [\hat{a}_m]_i d_{ijk} A_{m'} [\hat{a}_{m'}]_j A_{m''} [\hat{a}_{m''}]_k \\ &= A_{m'} A_{m''} [d_{ijk} [\hat{a}_m]_i [\hat{a}_{m'}]_j [\hat{a}_{m''}]_k] \\ &\equiv A_{m'} A_{m''} d_{\text{eff}}. \end{aligned} \quad (\text{A6})$$

Thus we can find d_{eff} for any chosen coupled polarization directions once we have d_{ijk} for the chosen frequency and temperature. The temperature- and frequency-dependent components can be approximated from Miller's rule^{35,40}:

$$\begin{aligned} d_{ijk}(\lambda, T) &= \epsilon_0 \delta_{ijk} \{ [n_i^{(2\omega)}]^2 - 1 \} \{ [n_j^{(\omega)}]^2 - 1 \} \\ &\quad \times \{ [n_k^{(\omega)}]^2 - 1 \}. \end{aligned} \quad (\text{A7})$$

We need just $n_j(\lambda, T_i)$ and the nearly constant Miller indices δ_{ijk} , given by³⁵

$$\delta_{ijk} = \begin{cases} ijk = & \delta(m^2/C) \\ 311 & -3.0 \times 10^{-2} \\ 322 & -3.2 \times 10^{-2} \\ 333 & -6.6 \times 10^{-2} \\ 223, 232 & -2.9 \times 10^{-2} \\ 113, 131 & -3.0 \times 10^{-2} \end{cases}$$

Finally, we point out that nonlinear coefficients can vary from crystal to crystal, depending on the crystals' quality or history. Poorly grown, damaged, or depoled crystals can have lower nonlinearities, so it is best to measure the nonlinearity for each crystal. The calculation of d above is most valuable for comparison of various configurations and for rough or upper-bound values of the nonlinear conversion.

We acknowledge financial support from the Centre National de la Recherche Scientifique (France) and the Provence-Alpes-Côtes-d'Azur Region. We thank J. C. Bernard for his technical contributions and Jean-Jacques Zondy for helpful discussions.

References

1. H. Katori, T. Ido, Y. Isoya, and M. Kuwata-Gonokami, "Magneto-optical trapping and cooling of strontium atoms down to the photon recoil temperature," *Phys. Rev. Lett.* **82**, 1116–1119 (1999).
2. H. Katori, M. Takamoto, V. G. Pal'chikov, and V. D. Ovsianikov, "Ultra-stable optical clock with neutral atoms in an engineered light shift trap," *Phys. Rev. Lett.* **91**, 173005 (2003).
3. Y. Bidet, B. Klappauf, J. C. Bernard, D. Delande, G. Labeyrie, C. Miniatura, D. Wilkowski, and R. Kaiser, "Coherent light transport in a cold strontium cloud," *Phys. Rev. Lett.* **88**, 203902 (2002).
4. U. Sterr, K. Sengstock, J.-H. Müller, and W. Ertmer, "High-resolution isotope shift measurement of the MgI 1S_0 - 3P_1 intercombination transition," *Appl. Phys. B* **56**, 62–64 (1993).
5. C. E. Simien, Y. C. Chen, P. Gupta, S. Laha, Y. N. Martinez, P. G. Mickelson, S. B. Nagel, and T. C. Killian, "Using absorp-

- tion imaging to study ion dynamics in an ultracold neutral plasma," <http://arxiv.org/abs/physics/0310017>, accessed 20 December, 2003.
6. Th. Udem, S. A. Diddams, K. R. Vogel, C. W. Oates, E. A. Curtis, W. D. Lee, W. M. Itano, R. E. Drullinger, J. C. Bergquist, and L. Hollberg, "Absolute frequency measurements of the Hg^+ and Ca optical clock transitions with a femtosecond laser," *Phys. Rev. Lett.* **86**, 4996–4999 (2001).
 7. Y. Takasu, K. Maki, K. Komori, T. Takano, K. Honda, M. Kumakura, T. Yabuzaki, and Y. Takahashi, "Spin-singlet Bose–Einstein condensation of two-electron atoms," *Phys. Rev. Lett.* **91**, 040404 (2003).
 8. T. P. Dinneen, K. R. Vogel, E. Arimondo, J. L. Hall, and A. Gallagher, "Cold collisions of Sr^* –Sr in a magneto-optical trap," *Phys. Rev. A* **59**, 1216–1222 (1999).
 9. T. Kurosu and F. Shimizu, "Laser cooling and trapping of alkaline earth atoms," *Jpn. J. Appl. Phys.* **31**, 908–912 (1992).
 10. X. Xu, T. H. Loftus, J. L. Hall, A. Gallagher, and J. Ye, "Cooling and trapping of atomic strontium," *J. Opt. Soc. Am. B* **20**, 968–976 (2003).
 11. M. Bode, I. Freitag, A. Tünnermann, and H. Welling, "Frequency-tunable 500-mW continuous-wave all-solid-state single-frequency source in the blue spectral region," *Opt. Lett.* **22**, 1220–1222 (1997).
 12. R. Paschotta, P. Kürz, R. Henking, S. Schiller, and J. Mlynek, "82% Efficient continuous-wave frequency doubling of 1.06 μm with a monolithic $\text{MgO}:\text{LiNbO}_3$ resonator," *Opt. Lett.* **19**, 1325–1327 (1994).
 13. W. J. Kozlovsky, C. D. Nabors, and R. L. Byer, "Efficient second harmonic generation of a diode-laser-pumped cw Nd:YAG laser using monolithic $\text{MgO}:\text{LiNbO}_3$ external resonant cavities," *IEEE J. Quantum Electron.* **24**, 913–919 (1988).
 14. J.-J. Zondy, "Experimental investigation of single and twin AgGaSe_2 crystals for cw 10.2 μm SHG," *Opt. Commun.* **119**, 320–326 (1995).
 15. V. D. Volosov, A. G. Kalintsev, and V. N. Krylov, "Phase effects in a double-pass frequency doubler," *Sov. Tech. Phys. Lett.* **5**, 5–7 (1979).
 16. M. Bode, "Abstimmbare Einfrequenz-Strahlquellen hoher Stabilität im infraroten, sichtbaren und ultravioletten Spektralbereich," Ph.D. dissertation (Universität Hannover, Hannover, Germany, 1999).
 17. R. Paschotta, "Einfach und doppeltresonante monolithische, Frequenzverdoppler für Experimente, in der Quantenoptik," Ph.D. dissertation (Universität Konstanz, Konstanz, Germany, 1994).
 18. V. D. Volosov and A. G. Kalintsev, "Optimum optical second-harmonic generation in tandem crystals," *Sov. Tech. Phys. Lett.* **2**, 373–375 (1976).
 19. L. K. Samanta, T. Yanagawa, and Y. Yamamoto, "Technique for enhanced second harmonic output power," *Opt. Commun.* **76**, 250–252 (1990).
 20. D. J. Armstrong, W. J. Alford, T. D. Raymond, and A. V. Smith, "Parametric amplification and oscillation with walkoff-compensating crystals," *J. Opt. Soc. Am. B* **14**, 460–474 (1997).
 21. J. P. Fève, J. J. Zondy, B. Boulanger, R. Bonnenberger, X. Cabirol, B. Ménaert, and G. Marnier, "Optimized blue light generation in optically contacted walk-off compensated RbTiO_3 – AsO_4 and $\text{KTiOP}_{1-y}\text{As}_y\text{O}_4$," *Opt. Commun.* **161**, 359–369 (1999).
 22. G. D. Boyd and D. A. Kleinman, "Parametric interaction of focused Gaussian light beams," *J. Appl. Phys.* **39**, 3597–3639 (1968).
 23. A. Ashkin, G. D. Boyd, and J. M. Dziedzic, "Resonant optical second harmonic generation and mixing," *IEEE J. Quantum Electron.* **QE-2**, 109–123 (1966).
 24. M. H. Dunn and A. I. Ferguson, "Coma compensation in off-axis laser resonators," *Opt. Commun.* **20**, 214–218 (1977).
 25. I. Juwiler, A. Arie, A. Skliar, and G. Rosenman, "Efficient quasi-phase-matched frequency doubling with phase compensation by a wedged crystal in a standing-wave external cavity," *Opt. Lett.* **24**, 1236–1238 (1999).
 26. R. W. Boyd, *Nonlinear Optics* (Academic, San Diego, Calif., 1993).
 27. A. Yariv, *Quantum Electronics* (Wiley, New York, 1989).
 28. I. Jovanovic, B. J. Comaskey, and D. M. Pennington, "Angular effects and beam quality in optical parametric amplification," *J. Appl. Phys.* **90**, 4328–4337 (2001).
 29. S. K. Wong, G. Fournier, P. Mathieu, and P. Pace, "Beam divergence effects on nonlinear frequency mixing," *J. Appl. Phys.* **71**, 1091–1101 (1991).
 30. H. Mabuchi, E. S. Polzik, and H. J. Kimble, "Blue-light-induced infrared absorption in KNbO_3 ," *J. Opt. Soc. Am. B* **11**, 2023–2029 (1994).
 31. E. S. Polzik and H. J. Kimble, "Frequency doubling with KNbO_3 in an external cavity," *Opt. Lett.* **16**, 1400–1402 (1991).
 32. L. E. Busse, L. Goldberg, and M. R. Surette, "Absorption losses in MgO -doped and undoped potassium niobate," *J. Appl. Phys.* **75**, 1102–1110 (1994).
 33. P. Lodahl, J. L. Sørensen, and E. S. Polzik, "High efficiency second harmonic generation with a low power diode laser," *Appl. Phys. B* **64**, 383–386 (1997).
 34. L. Shiv, J. L. Sørensen, and E. S. Polzik, "Inhibited light-induced absorption in KNbO_3 ," *Opt. Lett.* **20**, 2270–2272 (1995).
 35. I. Biaggio, P. Kerkoc, L.-S. Wu, B. Zysset, and P. Günter, "Refractive indices of orthorhombic KNbO_3 . II. Phase-matching configurations for nonlinear-optical interactions," *J. Opt. Soc. Am. B* **9**, 507–517 (1992).
 36. K. R. Vogel, "Laser cooling on a narrow atomic transition and measurement of the two-body cold collision loss rate in a strontium magneto-optical trap," Ph.D. dissertation (University of Colorado, Boulder, Colo., 1999).
 37. C. Batchelor, W. J. Chung, S. Shen, and A. Jha, "Enhanced room-temperature emission in Cr^{4+} ions containing aluminosilicate glasses," *Appl. Phys. Lett.* **82**, 4035–4037 (2003).
 38. J. Zimmermann, J. Struckmeier, M. R. Hofmann, and J.-P. Meyn, "Tunable blue laser based on intracavity frequency doubling with a fan-structured periodically poled LiTaO_3 crystal," *Opt. Lett.* **27**, 604–606 (2002).
 39. B. Zysset, I. Biaggio, and P. Günter, "Refractive indices of orthorhombic KNbO_3 . I. Dispersion and temperature dependence," *J. Opt. Soc. Am. B* **9**, 380–386 (1992).
 40. B. E. A. Saleh and M. C. Teich, *Fundamentals of Photonics* (Wiley, New York, 1991).